POLITECNICO DI TORINO

Collegio di Ingegneria Chimica e dei Materiali

Master's Degree in Materials Engineering

Master's Degree Thesis

Electrochemical characterization of Molybdenum disulfide membranes for the energy transition

Supervisors:
Mara Serrapede
Andrea Lamberti

Candidate:
Mattia Prandi

2024/2025

INDEX

ABSTRACT

Molybdenum disulfide (MoS_2) is a transition metal dichalcogenide with unique physical, chemical and electronic properties, making it a significant material in nanotechnology, electronics and catalysis. Its structure enables MoS_2 to be exfoliated into monolayers with high surface area, flexibility and distinct electronic characteristics. Due to its high chemical stability, mechanical strength and semiconducting properties, MoS_2 is widely explored for many applications. This work will focus on the potential of MoS_2 as a 2D active material for membranes applied in water purification and as electrodes for supercapacitors. The aims are to obtain free-standing membranes, to investigate the possibility of accelerating the hydrothermal reaction with the usage of microwaves and to use binders such as carboxymethylcellulose (CMC), hydroxypropylcellulose (HPC), polyvinylidene fluoride (PVDF) and graphene oxide (GO) to produce composite membranes. The most promising free-standing membrane was prepared with 2D MoS_2 synthesized via hydrothermal reaction mixed with GO (with a MoS_2/GO ratio of 2:1) to promote mechanical stability, then filtered by vacuum filtration and characterized as a free-standing membrane for the permselectivity of different ions and as electrode in Li-ion half-cells.

INTRODUCTION

Molybdenum disulfide (MoS_2) has emerged as a promising material for advanced membrane and electrode applications due to its two-dimensional structure and exceptional electronic, optical, and chemical properties. MoS_2 membranes exhibit selective permeability, making them suitable for water purification and gas separation, with the potential to enhance energy efficiency and resource recovery offering a multitude of solutions to problems such as water pollution and drinking water production with applications involving agriculture, industry and civil helping to fight climate change issues [1]. In electrochemical applications, MoS_2 serves as an efficient electrode material for batteries, supercapacitors and for hydrogen production.

The MoS_2 membranes have numerous advantages with respect to the other studied materials such as graphene oxide, including high water flux which results in lower pressure applied and so low energy consumption, they allow continuous separation, the simplicity of their scalability, the absence of additives, and the flexibility to be combined with other separation methods. Fouling tendency, limited membrane life, low flow selectivity and linear scale-up are the most typical restrictions, regardless of the membrane chemistry [2,3]. A membrane is required to have high selectivity and permeability and in recent years the growing demand for new technologies has led to the use of 2D materials as membranes (with the thickness of one or a few atomic layers). These materials offer significant improvements in water permeability, and anti-fouling thanks to increased hydrophilicity (passive) and catalytic effects (active) [4]. In addition, they are very versatile and can be modified/functionalized to optimize properties such as hydrophobicity, morphology, thickness [5]. Water desalination is the most promising method of creating an infinite water supply. It offers a good prospective solution to the abundance of seawater, which is inaccessible for drinking. It involves removing salts and other dissolved contaminants from various sources, including surface and groundwater, industrial and municipal wastewater.

Membrane desalination uses a semi-permeable membrane (molybdenum disulfide, graphene etc.) to filter the water, allowing it to pass through and retain salts and other minerals, the common filtration techniques are pressure driven separation processes as nanofiltration (NF), reverse osmosis (RO), ultrafiltration (UF) where the difference lies in the filtration capabilities (UF 0.01-0.1 μm, NF 0.001-0.01 μm, RO 0.0001 μm) , and electrodialysis a process that uses electric fields to force ions through cation-exchange membranes (CEM) and anion-exchange membranes (AEM) [6,7].

Regarding the energy transition, sustainable energy systems are increasingly demanded, and they are reliant on advanced energy storage technologies, which are essential for balancing supply and demand, integrating renewable energy sources, and enhancing grid stability [8]. The central part to these technologies is the choice of electrodes and energy storage materials, which plays a critical role in determining the efficiency, capacity, and longevity of storage devices such as batteries and supercapacitors. Modern energy storage materials must meet the dual demands of high energy density and rapid charge-discharge capabilities while remaining environmentally friendly and economically viable [9]. Innovations in materials science,

particularly with the development of nanostructured and two-dimensional materials, are driving significant improvements in their performance. For instance, materials for lithium-ion technology and emerging alternatives, including sodium-ion and metal-organic frameworks, are being explored for their potential to enhance energy density and to reduce costs [10]. Furthermore, electrodes made from materials like graphene, molybdenum disulfide (MoS_2), and transition metal oxides are gaining attention for their unique properties, such as high conductivity and large surface area, which contribute to a better charge transfer and overall increased efficiency [11]. As the demand for energy storage solutions continues to grow, research and development in this field are pivotal for facilitating a smooth transition to renewable energy sources, ensuring that energy storage systems can effectively support the shift toward a low-carbon future.

Similarly, the development of new materials for electrocatalysis is a phenomenon that is growing hand in hand with the population due to the high energy demand and the need to introduce more fossil-free based alternative energy production methods. The applications are many: conversion of molecules (CO, CO_2, H_2O, N_2) into high value-added products (H_2, ammonia, hydrocarbons...). New materials and nanostructures are proposed as alternatives (even if less efficient) to Platinum because of its huge cost [12].

This work reviews the current state of research on MoS_2 membranes and electrodes, highlighting their fabrication methods, scalability, performance metrics, and future directions for enhancing their functionality in energy and environmental applications. The integration of MoS_2 with other materials, such as graphene oxide, is also discussed.

1 Inorganic membranes in the energy transition

Inorganic membranes are porous or non-porous materials made from non-organic substances such as metals, ceramics, carbon, or glass. They are extensively used in various applications requiring durability, high-temperature operation, and chemical resistance, including gas separation, water treatment, and catalysis. These membranes offer distinct advantages over organic polymer-based membranes [13]. Inorganic membranes can withstand harsh chemical environments (acidic, alkaline, or oxidizing) and high temperatures, making them suitable for industrial processes in more extreme conditions where polymeric membranes can't be applied thank to their high thermal and chemical stability. Mechanical strength another big advantage of inorganic membranes, their robustness, derived from the high modulus and resistance of the inorganic material, allows them to function under high-pressure conditions, ensuring reliable performance over long periods. They are also able to obtain high selectivity and permeability since their pore sizes can be tuned at the molecular or atomic scale for precise separation processes. The inorganic membranes can be categorized in three main types:

- Porous Membranes: these membranes feature micro-, meso-, or macropores and they are used in ultrafiltration, microfiltration, and nanofiltration. An example are ceramic membranes applied for water treatment [14].

- Non-Porous Membranes: they have dense structures that separate molecules based on diffusion. An example are Palladium membranes for hydrogen purification [15-17].

- Hybrid Membranes: Combining inorganic materials with polymers, obtaining composite with enhanced performance and functionality [18,19].

Inorganic membranes are part of the advanced separation technologies and continue to evolve with the integration of nanotechnology and material science. Nanostructured materials are under the studies of researchers to produce inorganic membranes with 2D layered materials with even better performances than the one we currently use in the industry [20].

These are the most studied materials used in nanostructured inorganic membranes:

- Nanoporous Ceramics: Materials like silica, alumina, or titania are structured with nanoscale pores, useful for ultrafiltration and gas separation in harsh conditions. Usually prepared with sol-gel synthesis but with lack of reproducibility, the alternative is a more expensive technique as CVD [21].

- Carbon-Based Nanostructures: Graphene oxide (GO) and carbon nanotubes (CNTs) are employed to create ultrathin, highly selective membranes capable of fast water transport with high selectivity of ions [22].

- Metal-Organic Frameworks (MOFs): MOFs, which are the most known synthesized porous crystalline materials, are incorporated into membranes for applications like CO_2 capture and gas separation but also liquid separation processes [23,24].

- Transition Metal Dichalcogenides (TMDs): layered 2D materials such as molybdenum disulfide (MoS_2) and tungsten disulfide (WS_2), they showcase the same capabilities of the carbon based 2D nanostructured membranes, but with higher chemical stability and higher potential in water treatment promising to achieve ultrafast molecule separation and high-performance energy storage [25].

The main applications for these nanostructured membranes are:

- Water Treatment: Nanostructured membranes are used for desalination, heavy metal removal, and organic pollutant filtration due to their high selectivity and resistance to fouling. The main industries are water management industry, secondary and tertiary wastewater treatment, membranes bioreactors [26].

- Ionic Exchange Membranes: used to separate and recover ions by selectively allowing the transport of the cation (cation exchange membranes) or anion (anion exchange membranes) and recover resourceful ions with low energy investment [27].

- Gas Separation: Efficient separation of gases like hydrogen, methane, or CO_2 is possible through nanoporous membranes. Usually used zeolite or silica-based membranes [28].

- Energy Storage and Conversion: Membranes incorporating nanostructured materials are used in batteries, fuel cells, capacitors and reverse electrodialysis to optimize ion transport [29].

1.1 Water treatment

The membrane technology is a separation process that allows only some species to pass through, allowing to separate a fluid like water from impurities as particles, bacteria, viruses, molecules, and even atoms as heavy metals and salts.
One of the most studied 2D materials to produce membranes for water treatment is graphene and its derivatives, such as graphene oxide (GO) and reduced graphene oxide (rGO) [30]. Graphene is a single-atom thick membrane (0.34 nm) that has been shown to have higher flow rates than conventional membranes because of the thin film (potentially monolayer for porous graphene) that reduce the transport path length of the water molecules [31,32].
There are other 2D materials such as MoS_2, MXene, boron nitride [33], metal-organic structures [34] and covalent organic frameworks [35,36] that are emerging for desalination applications [37,38].

There are three ways to produce membranes with 2D materials: monolayer porous, stacking, and composite membranes (**figure 1.1**). Monolayer membranes are produced by creating pores (**figure 1.2b**) so that the filtration takes place with the passage of water through the pores. This porosity complies with the measurement limits to allow the water molecules to pass through, but at the same time to retain the ion. The required porosity ranges from 15 to 75 $Å^2$ depending on the functionalization of the pore and the material chemistry, but some materials like MoS_2

seems to perform way better (**figure 1.2a**) [39]. Chemical functionalization of a graphene nanopores (e.g., addition of hydroxyl groups) showed to improve the permeability, but is has been observed a lower desalination efficiency [40].

The membranes produced through the stacking of 2D materials can filter the water through the capillary channels that are formed between the flakes. Their production is much simpler, and it is more scalable and faster than to produce nanoporous membranes because it is possible to employ vacuum filtration systems [41].

Composite membranes are prepared with 2D materials like GO, MoS_2, or MXenes and embedded into polymeric matrixes (PVDF, HPC, CMC, polyamide, polysulfone) to create thin-film nanocomposites.
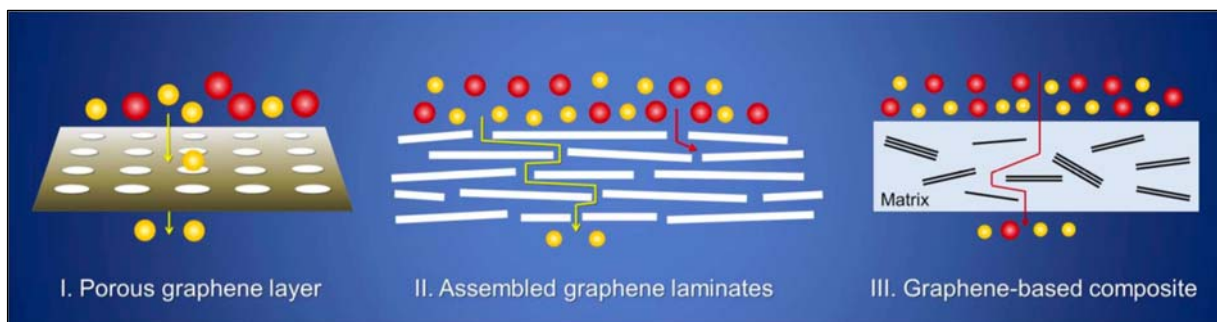
Figure 1.1: The three types of filtration membranes that can be produced: I) porous, II) assembled by stacking, III) composite.
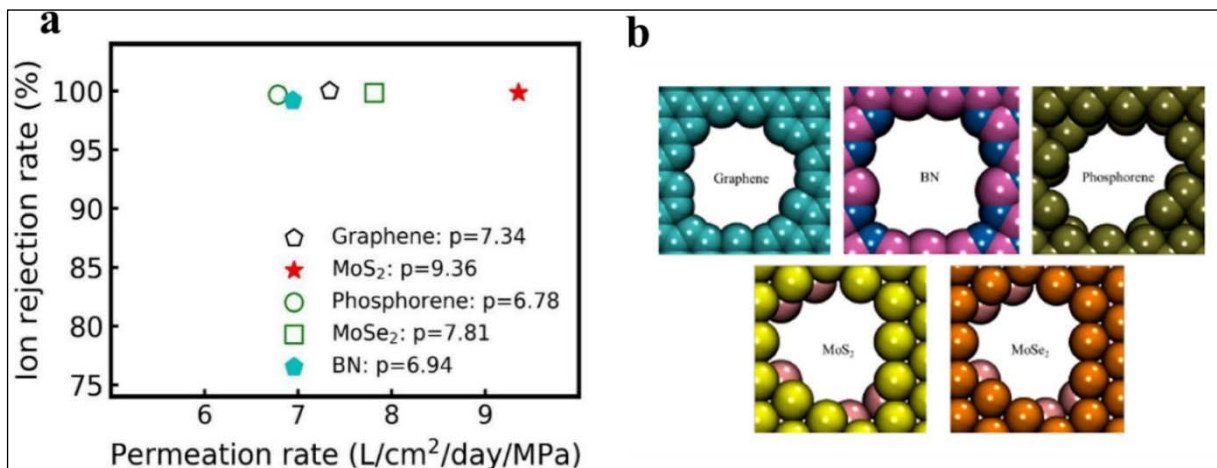
Figure 1.2: (a) permeability and ion retention of different 2D materials, (b) nano pores in 2D materials [5].

1.2 Hydrogen Evolution Reaction (HER)

Hydrogen Evolution Reaction (HER) is among the most interesting catalysis reactions capable of producing H_2, an alternative fuel to fossil fuels, using only H_2O as a starting molecule [42].

$$2H^+ + 2e^- \rightarrow H_2$$

The reaction involves a transfer of two electrons and can take place according to three mechanisms where * is a site on the electrode surface, H* is a hydrogen adsorbed on a site, H^+ is a hydrogen ion, e- is the electron transferred [43,44]:

Volmer: $H^+ + e^- + * \rightarrow H*$

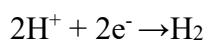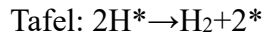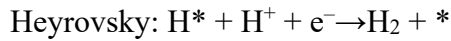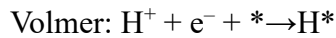Heyrovsky: $H* + H^+ + e^- \rightarrow H_2 + *$

Tafel: $2H* \rightarrow H_2 + 2*$

The reaction rate is influenced in relation to Sabatier's principle: if hydrogen binds too much to the surface it will not be able to desorb, on the contrary a weak adsorption will lower the reaction rate, in **figure 1.3** the reaction rate is expressed as exchange current density j_0 (A/cm2) which represent the intrinsic activity of the catalyst for the HER while the x-axis represent the Gibbs free energy change associated with hydrogen adsorption on the catalyst surface ΔG_{H*} (eV). When the free energy is near zero, indicates an optimal binding energy for hydrogen, as it balances adsorption and desorption rates, making the catalyst highly effective for HER. In density functional theory (DFT) calculations the edge sites MoS2 reaches a ΔG_{H*} of 0.08V (**figure 1.3**) at 50% hydrogen coverage which is close to the optimal 0V and potentially competitive with the most common but expensive metal catalysts [45].
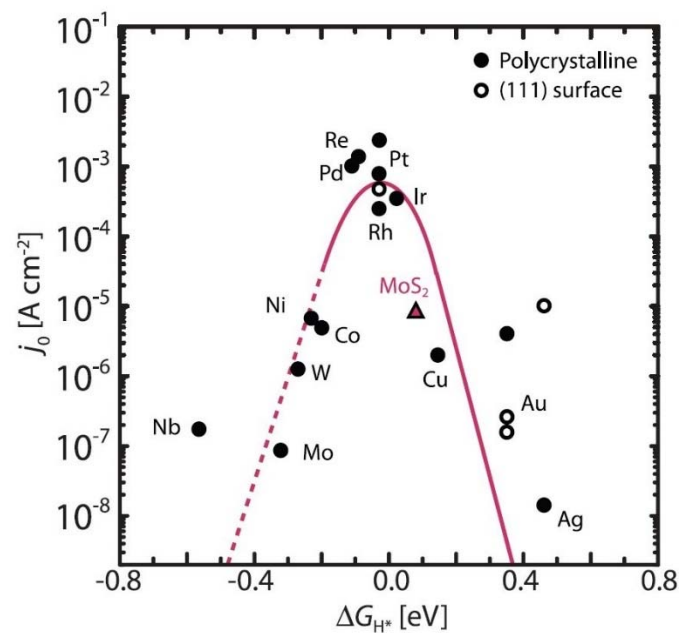

Figure 1.3: Sabatier principle with some known catalysts represented [46].

1.3 Energy storage

The most popular methods of storing electric charge are Lithium-ion and Sodium-ion batteries (LIBs and SIBs), solid state batteries that use a solid electrolyte instead of a liquid one, and capacitors for a fast store and release of energy.

- Lithium-Ion Batteries Li-Ion are one of the most popular forms of energy storage, used in portable electronics, electric vehicles (EVs), and grid storage. Their advantages are high energy density, good cycle life, and efficiency, but the challenges are limited by thermal runaway risks, degradation over cycles, and dependency on critical raw materials like lithium and cobalt.

- Sodium-ion batteries use sodium ions instead of lithium, offering a more abundant and environmentally friendly alternative. The advantages are lower material cost and potential for high scalability, but the challenges are lower energy density compared to Li-ion and ongoing research to improve cycle life and efficiency. Moreover, the real environmental impact on large scale production line has to be carefully evaluated because at the moment different data show a bigger impact than LIB's production, but the comparison is between the large-scale production of LIBs and the pilot-scale production of NIBs which has still a lot of potential on increasing the energy efficiency of the process [47,48].

- Solid-State Batteries use a solid electrolyte instead of a liquid one, improving safety and energy density, their advantages are a reduced risk of leakage and fire, higher energy density while their challenges are high production costs, difficulties in the scaling up and reduced power.

- Electric Capacitors are essential components in electronic circuits, known for their ability to store and release electrical energy. They are widely used in various applications, from simple electronic circuits to advanced energy storage systems, due to their fast charge and discharge rates. Capacitors work on the principle of storing energy in an electric field created between two conductive plates separated by a dielectric material.

But there are new generations of storage systems such as supercapacitors: they are energy storage devices that bridge the gap between conventional capacitors and batteries providing high power density with a good compromise in terms of energy storage. There are different types of supercapacitors, working with different principles: (**figure 1.4**).

- Electrostatic double-layer capacitors (EDLCs) are a type of supercapacitor that stores energy through the formation of an electric double layer at the interface between the electrode and electrolyte. Unlike batteries, EDLCs store energy electrostatically, without chemical reactions, which gives them unique performance characteristics.

When a voltage is applied, ions in the electrolyte are attracted to the surface of the oppositely charged electrodes. This creates two layers of charge (positive and negative), separated by a molecular-sized distance, forming the "double layer".

- Pseudocapacitors (PCs) can store in a pseudo-capacitive way (**figure 1.4**), overcoming the limits of the batteries and capacitors previously mentioned. Pseudo-capacitive is a term that define mechanisms that behave like an EDLC, but they also involve multiple and highly reversible redox reactions while allowing charge transfer processes between the electrolyte and the electrode contributing to additional capacitance beyond the EDLC [49].

- Hybrid capacitors (HCs) are type of supercapacitors that combine features of electric double-layer capacitors (EDLCs) and pseudocapacitors to balance high energy density, power density, and longevity. The result is a device with the complementary properties of EDLCs (fast charging, long life) and pseudocapacitors (higher energy density through faradaic reactions).

Another way the literature categorizes these devices is how the electric charge can be accumulated, the mechanism can be Faradic or non-Faradic, and it describes what happens to the electrode, how the charge is transferred from the electrolyte to the electrode and vice versa.
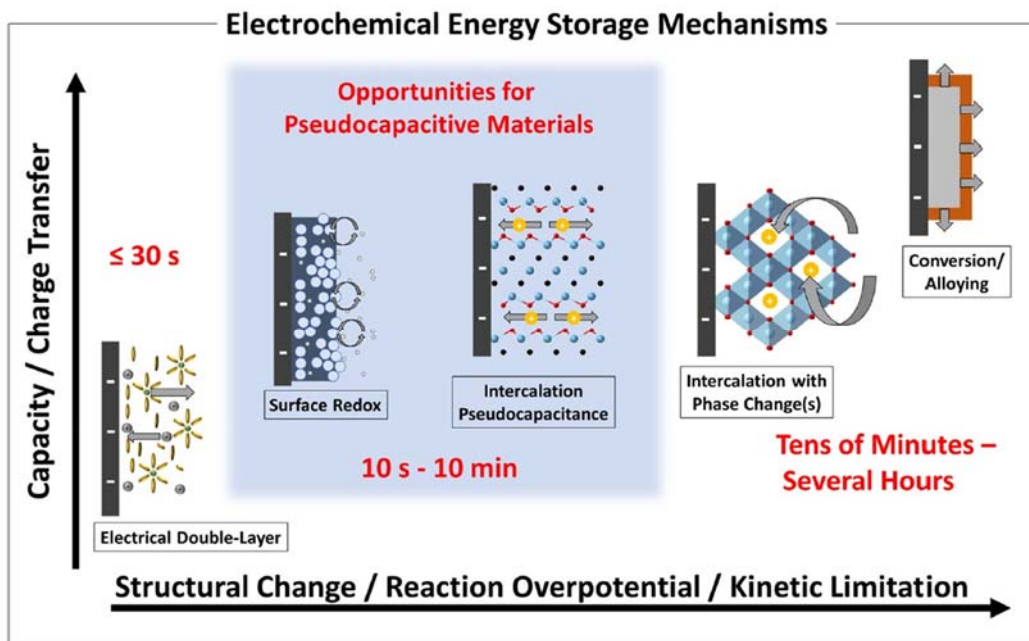

Figure 1.4: Charge storage mechanisms [49].

In a Faradic process, the charges move along the electrode and do not remain on its surface, this mechanism means that, when a constant current is applied, the voltage will tend to a constant value (in the case of battery materials) or to an almost-linear decay (pseudocapacitors). An ion must reach the electrode, oxidize or reduce to another species, and consequently move in (adsorption, intercalation or alloying) or away (redox-flow batteries) from the electrode surface.

In a non-Faradic process, however, the charges remain on the surface of the electrode giving a surface charge accumulation such as the double-layer. Since the surface is a limiting factor in non-faradic processes (EDLCs), nanostructured materials capable of developing considerable surface areas are exploited.

2D MATERIALS: MoS$_2$

MoS$_2$ is a Transition Metal Diacalcogenide (TMD)that belongs to the layered materials in which the transition metal layers are between two layers of chalcogen atoms, whose formula is MX$_2$ where M is the transition metal (of group IV, V or VI) and X the chalcogenide [50]. The structure of MoS$_2$, as with other TMDs, consists in bonded layers of S-Mo-S, with a layer of Mo atoms sandwiched between two layers of S atoms, (**figure 2.1**). These layers are held together only by weak Van der Waals forces, but strong covalent forces hold the individual atomic interlayers [12]. A single-layer MoS$_2$ has a Young's modulus of 200-300 GPa that can be compared to steel [51]. The band gap can move from 1.9 eV in bulk to 1.2 eV single layer due to quantum confinement [52,53] and changes from a direct to an indirect gap in single-layer structures, while the distance between MoS$_2$ layers is around 0.615 nm with a spacing of 0.290 nm (**figure 2.1**) these distances can vary depending on hydration, functionalization and intercalation on ions.
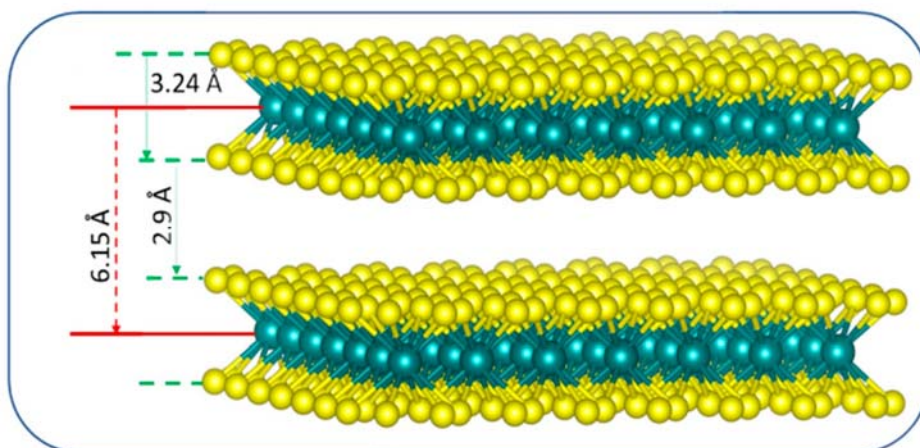
Figure 2.1: 3D representation of the 2H-MoS$_2$ with interlayer distance, spacing and thickness of the layer [68].

The MoS₂ exists in trigonal (T), hexagonal (H), and rhombohedral (R) structures, of the many there are three main structures 1T, 2H and 3R, where the phase 1T forms an octahedral structure, while 2H and 3R in a trigonal prismatic structure, as shown in **figure 2.2**.

- 1T-MoS₂ has one S-Mo-S layer per cell unit, with octahedral coordination. It exhibits a metallic behaviour and has peculiar properties in comparison to others forms like Pauli paramagnetism and a negative temperature coefficient for electronic conductivity [12]. This phase is metastable, and it is found as monolayers.
- 2H-MoS₂ belongs to the hexagonal system and is usually the most stable phase. The electronic structure 2H-MoS₂ is semiconductive. This phase is more thermodynamically stable, making it the natural form of MoS₂, especially at room temperature and in bulk [54].
- 3R-MoS₂ has rhombohedral symmetry and is composed of three layers, it is also semiconductor.

Figure 2.2: MoS₂ structures (1T,2H,3R) with a scheme of their coordination Mo-S, top view and stacking sequence [55].

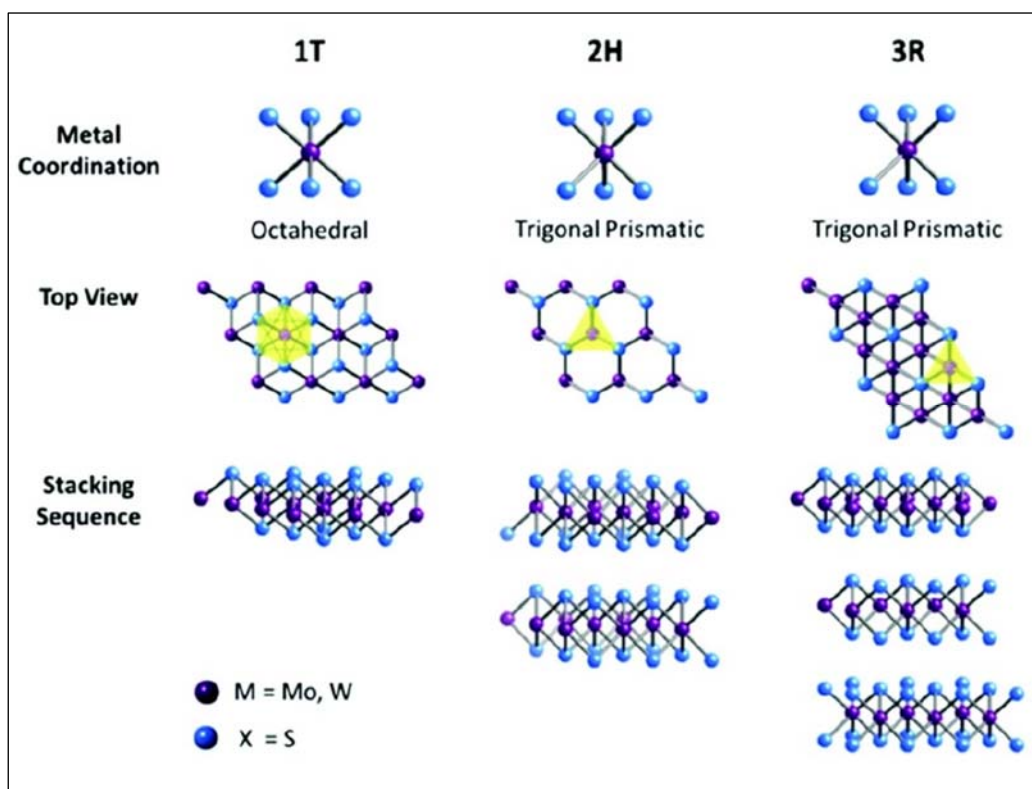## 2.1 MoS$_2$ characteristics and production methods

2D MoS$_2$ is considered a superior electrode material because of its electronic properties, its high specific capacity up to 670mAh/g [56] (more electric charge per gram of material), low overpotential compared with other materials and close values to the most used catalyst like platinum [57] (higher redox efficiency), stability over time.

The applications go from the most studied Lithium-ion batteries (LIBs) to other electrolytes as Sodium-ion batteries (SIBs) and supercapacitors, but the redox reactions can cause volume changes for 2H-MoS$_2$ that will lower its cycling stability.

The electrode performances are especially interesting for the 1T-MoS$_2$ phase because it is metallic even if it's not as electrically conductive as conventional metallic electrodes and the measured values of its electrical conductivity can vary because of influencing factors such as layer thickness and defects (**Table 2.1**).

Table 2.1: electrical conductivity of MoS$_2$ 1T, 2H (a [58] and b [59] are different sources) and other metals used for electrodes.

	Conductivity σ	
	a	b
1T-MoS$_2$	2 S/cm	100 S/cm
2H-MoS$_2$	10^{-4} S/cm	0.15 S/cm
Cu	580000 S/cm	
Al	61% Cu	
Ni	24% Cu	
Stainless steel	14500 S/cm	

MoS$_2$ nanosheets exist either the 2H or 1T phase, and they can be changed from one to the other by thermic annealing (1T to 2H) or atomic interlayer creep caused by atomic intercalation (2H to 1T) [60]. 2H is the phase mainly used for membrane separation, catalyst and energy storage, but MoS$_2$ can exist in different 2D structures such as nanosheets and nanoribbons. There are different techniques to synthetise flakes, each one has some pros and cons, the two approaches are bottom-up and top-down.

Top-down approaches are all exfoliation techniques such as mechanical, liquid and sputtering while bottom-up is used to obtain the 2D nanosheets using a precursor and expensive techniques such as PVD, CVD, ALD, but also simpler ones like hydrothermal and solvothermal synthesis.

Solvothermal processes

The solvothermal process is an effective method for synthesizing molybdenum disulfide (MoS$_2$) nanosized, enabling the control over the morphology, size, and crystallinity of the resulting MoS$_2$. This method typically involves using a molybdenum precursor and a sulfur source in a solvent at elevated temperatures and pressures in a sealed autoclave. Solvothermal synthesis is particularly useful for creating MoS$_2$ with specific nanostructures, including

nanosheets and nanoflowers, which have applications in catalysis, electronics, and energy storage. This method can be found in the production of MoS_2/C and $MoS_2/graphene$ nanocomposites as well [12]. The solvothermal process employs a solvent capable of solubilize the reagents of the synthesis, when water is used the process is called hydrothermal. Other solvents employed are usually ethanol and DMSO.

Layer by layer exfoliation

A process used to form 2D materials from bulk, also called the "scotch method", consists of peeling off the layers of material by simply overcoming the weak Van der Waals attractions. It is the simplest method to produce MoS_2 2D but limited by the defectiveness and scalability of the process [61]. Repeating this process can produce flakes with varying shapes, sizes, and thicknesses (number of layers).

Liquid phase exfoliation

Liquid-phase exfoliation of MoS_2 begins with bulk MoS_2 and produces flakes with varying shapes, sizes, and thicknesses (number of layers). While this method can generate larger quantities compared to tape-assisted exfoliation, the quality of the flakes is generally lower. There are two main approaches to achieve exfoliation in solution:

- Mechanical Exfoliation Methods:
  These techniques rely on physical processes such as sonication, shearing, stirring, grinding, or bubbling to separate the MoS_2 layers. Although primarily physical, some chemical interactions may also play a role. For instance, surfactants like sodium deoxycholate (SDC) or chitosan can be added to prevent cohalescence of the exfoliated flakes. Although this method significantly improves the yield compared to mechanical tape exfoliation, the efficiency is still insufficient for industrial-scale applications. A simple method of exfoliation can be with the use of salts (sodium tartrate, potassium sodium tartrate and potassium ferrocyanide) in isopropyl alcohol [62].

- Chemical and Electrochemical Intercalation:
  This approach involves atomic intercalation, where a chemical species such as lithium is introduced between MoS_2 layers to expand the interlayer spacing. This facilitates subsequent exfoliation through mechanical means, such as sonication [63]. In some cases, electrolysis is used to generate bubbles, which penetrate material interfaces and aid exfoliation [55].

Physical Vapour Deposition (PVD)

PVD of MoS_2 refers to the synthesis or coating of molybdenum disulfide (MoS_2) thin films using physical vapour deposition techniques.

Chemical Vapor Deposition (CVD)

It offers the possibility of depositing different substrates (Si, SiO$_2$, Al$_2$O$_3$, ...), even with metal-organic precursors (MOCVD). Single-layer MoS$_2$ films or with a few layers can be prepared. Versatile also from the point of view of the morphology to be obtained (lamellae, fullerene-like structures) [12]

Atomic Layer Deposition (ALD)

ALD is a powerful technique for depositing molybdenum disulfide (MoS$_2$) thin films with precise thickness control and excellent uniformity. ALD enables deposition of MoS$_2$ monolayers or few-layer films with atomic precision, which is especially useful for applications in electronics, catalysis, and sensors where controlled layer thickness and surface uniformity are critical. ALD is a scalable process, allows good control in thickness and good coverage of complex 3D structures but it is very expensive for mass production, and other challenges are high crystallinity and low defects.

Microwave assisted synthesis

Microwave-assisted synthesis is an efficient method for producing MoS$_2$ nanostructures due to its rapid heating and energy transfer capabilities. Compared to traditional hydrothermal synthesis, which often takes from 12 to 24 hours, microwave synthesis can significantly shorten the reaction time—typically reducing it to 30 minutes. This method provides improved control over morphology, yielding thinner and more uniformly structured MoS$_2$ nanosheets with smoother edges [64-76].

Microwave plasma

Reaction of precursor gas in a microwave-generated plasma in a quartz tube; the reactants are Mo(CO)$_6$ and H$_2$S in Argon. With frequencies of 0.915 GHz and 2.45 GHz [77].

2.2 MoS$_2$ as electrode for storage

MoS$_2$ has gained significant attention as an electrode material for energy storage systems such as batteries and supercapacitors. Its unique properties make it a promising candidate for improving the performance of energy storage devices. Its structure allows high ion intercalation capacity, large active area enhancing storage efficiency, electrical conductivity particularly for the 1T phase, chemical stability and reversible intercalation of monovalent ions, making it suitable for LIBs and SIBs. It is also suitable for supercapacitors thanks to its high volumetric capacitance up to 700 F/cm^3 for aqueous electrolytes compared to the 300 F/cm^3 of graphene [78] and capacity up to 300-350 mAh/g at 0.1 mV/s for SIBs and LIBs [79].

2.3 MoS$_2$ as electrocatalyst

The MoS$_2$ is a very promising electrocatalyst for hydrogen evolution reaction (HER), [80], small flakes are the desired nanostructure to achieve better activity since the edges are demonstrated to be more active than the basal plane. They allow the adsorption of H$^+$ to be more effective thanks to uncoordinated atoms of sulphur [68]. The edges between two crystalline domains are extremely active as well [81]. This material is for sure promising even if worse than platinum as a catalyst: the higher cost of platinum is guiding the research towards more affordable catalyst as alternatives. The 1T-MoS$_2$ seems to be even more competitive than the 2H-MoS$_2$ for HER since also his basal plane plays an important role in its activity by conducting and so improving the charge transport to the edge sites and the kinetics of the reaction [82]. The **figure 2.3** showcases how the 1T-MoS$_2$ has HER performance closer to platinum than the 2H-MoS$_2$, a lower Tafel slope suggests that the hydrogen absorption is closer to equilibrium and the polarization curves shows a HER activity quite close to the platinum for 1T-MoS$_2$ reaching good current densities at low overpotentials.
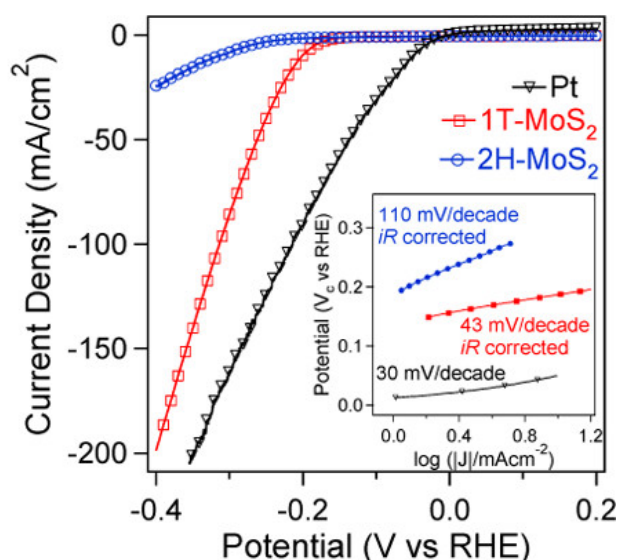
Figure 2.3: polarization curves and Tafel plots of 1T-MoS$_2$ compared with 2H-MoS$_2$ and platinum [83].

2.4 MoS$_2$ in membranes

Membranes of two-dimensional nanosheets of MoS$_2$ stacked in layers have recently shown great promises for water filtration. Currently, reported water flows vary significantly, while the structure and properties responsible for MoS$_2$ nanochannels are largely unknown.

The interlayer of MoS$_2$ membranes in aqueous solution is maintained by Van der Waals forces and hydration forces, thus ensuring the aqueous stability of MoS$_2$ membranes without the need

for cross-linking and the high-water flow (30-250 $Lm^{-2}h^{-1}bar^{-1}$) of MoS_2 can be attributed to the low hydraulic resistance of the smooth and rigid MoS_2 nanochannels [41].

The layered 2D structure together with its chemical stability and its hydrophilicity is what makes MoS_2 a desirable material for membranes, making it easier to separate water from contaminants. Another interesting application is for cation exchange membranes (CEM), because its natural negative charge allows a preferential transport of cations, useful in fuel cells or in devices to recover metal ions.

Both MoS_2 and graphene have excellent performance for water desalination, and several literature studies have shown that MoS_2 is better than graphene and its derivatives because of chemical stability, higher water permeability, and linear dependence between water permeability and pressure applied suggesting the MoS_2 membranes do not get deformed [84]. Molecular dynamics studies [85] have also compared the performance of porous graphene and MoS_2 nanosheet, and the results show that MoS_2 performs better than graphene in terms of water permeability. In fact, MoS_2 membrane shows consistent higher water flux, in the left graph in **figure 2.4** it can be observed how the water velocity (black line) it considerably higher in proximity of the pore center.
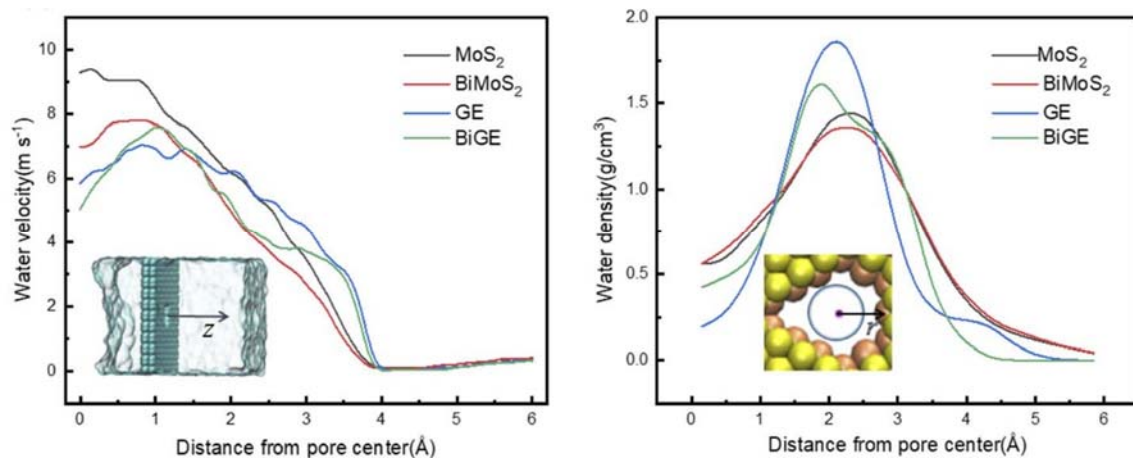

Figure 2.4: Axial water velocity (left) and mass density of water molecules (right) through the pores of the membranes of monolayer and bilayer MoS_2 and graphene (GE) [85].

INSTRUMENTATION, SYNTHESIS, AND CHARACTERIZATION TECHNIQUES

3.1 Instrumentation and materials

3.1.1 Instrumentation

Glove Box

The Glove Box is a chemical fume hood in a sealed environment where it is possible to handle reactive materials or materials susceptible to oxygen and water (**figure 3.1**). Inside, there is an inert gas (Argon or Nitrogen) and it is possible to monitor in real time through a display the pressure and the content of water and oxygen in ppm (part per millions). The black gloves in "butyl" allow the operator to handle the material inside while the introduction and the withdrawal of things is possible through one of the two pre-chambers of different size. Inside them, the introduced material is "washed" with degassing cycles applying vacuum and then refilling the pre-chamber with the inert gas for at least three cycles.

Figure 3.1: Glove Box used in the laboratory.

Thermostatic oven

Used to remove humidity from material and tools, usually set at 60 °C with forced air recirculation (**figure 3.2**).

Figure 3.2: Thermostatic oven used in the laboratory.

Synthesis muffle oven

It is a high temperature furnace typically made of refractory ceramics (alumina) for material synthesis, annealing, calcination, or ash testing (**figure 3.3**).

Figure 3.3: Muffle oven in the laboratory.

Ultrasonic bath

The ultrasonic bath is a cleaning device that transmits high-frequency sound waves through liquid to clean laboratory equipment, but also it helps to solubilize or disperse materials into

solvent (**figure 3.4**). Usually works at 44kHz and the agitation of water causes cavitation, a molecular implosion strong enough to remove contaminants from surfaces.

Figure 3.4: Ultrasonic cleaner used in the laboratory (RS PRO 100W).

Lyophilizer

Lyophilizing is a low temperature dehydration process, involves freezing the sample and lowering the pressure causing the removal of ice through sublimation. The equipment used is LIO−5P DIGITAL 5 Pascal, Italy (**figure 3.5**).

Figure 3.5: lyophilizer used in the laboratory.

Centrifuge

The centrifuge is a laboratory device that uses centrifugal forces to separate fluids from solids or various components of a fluid causing denser materials or fluids to accumulate towards the bottom of the falcon tubes (**figure 3.6**).

Figure 3.6: centrifuge used in the laboratory.

Vacuum oven

The vacuum oven (model Buchi® Glass Oven B-585) is used to remove water and other solvents from the sample by applying vacuum and raising the temperature (**figure 3.7**).

The oven consists of some glass tubes one inside the other, the inner one is where the sample is placed, and it can be linked to the vacuum pump through a tap.

Figure 3.7: BUCHI oven used in the laboratory.

A vacuum filtration system is a laboratory apparatus used for separating solid particles from liquids using a vacuum. It operates by creating a differential pressure between the filtration system and the surrounding atmosphere, which forces the liquid through a filter, leaving the solid particles behind. This system is commonly used in chemistry, biology, and environmental science for applications that require rapid and efficient separation of solids from liquids. This set up (**figure 3.8**) is common in laboratories for producing membranes or separating solid content from liquid. It consists in a vacuum pump that creates the vacuum by removing air from the system, creating a lower pressure inside the filtration apparatus with respect to the surrounding environment. A filter flask, a special container that collects the liquid that passes through the filter, usually made of glass, is designed to withstand the vacuum pressure. The filter funnel is the funnel into which the solid-liquid mixture is poured, it sits on top of the filter flask and where the filter paper or the membrane that separates the solids from the liquid sits. The filter paper or membrane and the choice of filter paper or membrane depends on the size of the particles being filtered. The tubing connects the vacuum pump to the filter flask, facilitating the flow of air and creating the necessary vacuum pressure. The glass filter is a filter with higher porosity where it is possible to lay another filter of the needed porosity [86].

Figure 3.8: Vacuum Filtration System.

Potentiostat/Galvanostat

A potentiostat/galvanostat is an electronic device used to control the voltage between a working electrode and a reference electrode in an electrochemical cell, while measuring the resulting current through the working electrode and the counter electrode. It is essential in electrochemical research, and it is widely used in applications such as corrosion studies, battery testing, material characterization and sensor development.

The instrument used is an Metrohm Autolab M302 potentiostat/galvanostat (**figure 3.9**) and uses the Nova 2.1 software. The studied membrane was measured for electrochemical characterization and membrane filtration performance (permselectivity,). Permselectivity was measured at open circuit potential (OCP), ion conductivity was measured with Electrochemical Impedance Spectroscopy (EIS), then the half-cell setup made into coinc ells was tested with cyclic voltammetry at different scan rates (CV) after checking the stability with an EIS.
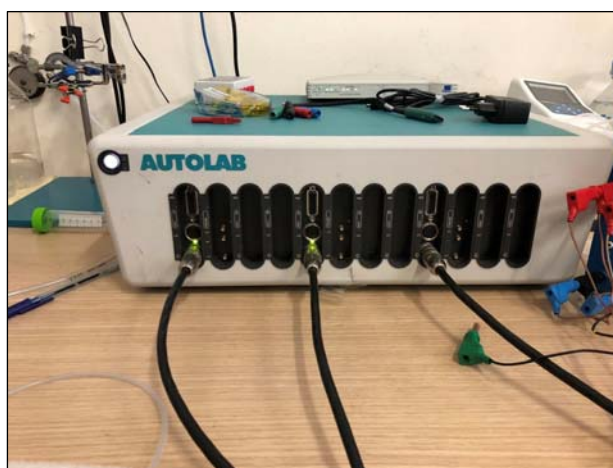
Figure 3.9: AUTOLAB potentiostat used in the laboratory.

Microwave oven (FlexiWAVE MA 186)

A laboratory microwave oven is a specialized microwave designed for scientific applications, distinct from typical household microwaves. Laboratory microwaves are engineered to handle specific requirements for consistent and controlled heating for digestion, extraction, and other processes that need precise energy application (**figure 3.10**).
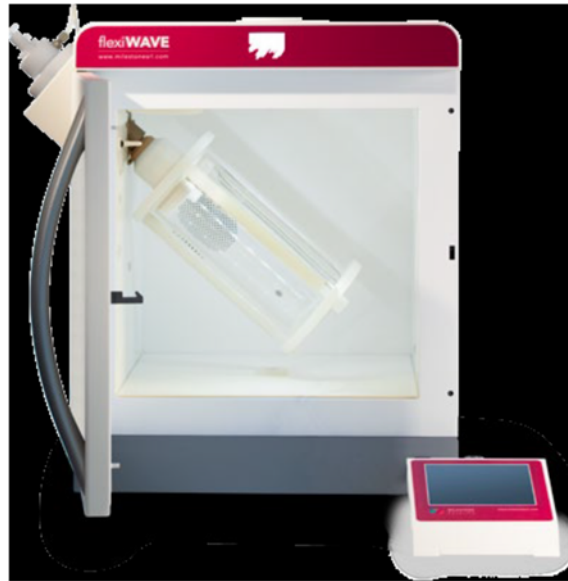
Figure 3.10: Microwave oven

Doctor Blade

The doctor blade is a device used in various industrial and laboratory applications to control the amount of ink, coating or material applied to a surface (**figure 3.11**). A blade made of metal is connected to micrometers to set up a precise gap between the blade and the surface. Then it is automatically or manually moved to spread the ink over the surface with the desired thickness.

Figure 3.11: model of the doctor blade in the laboratory.

Steel Autoclaves

A steel autoclave is a high-pressure, high-temperature vessel used to carry out various chemical, biological, and industrial processes that require controlled conditions. It is made from stainless steel, and it stores a 25 mL Teflon reactor.

3.1.2 Materials

Phosphomolybdic acid (PMA)

$H_3[P(Mo_3O_{10})_4]$, (1826 g/mol) as a source of Molybdenum for the hydrothermal synthesis (**figure 3.12**).
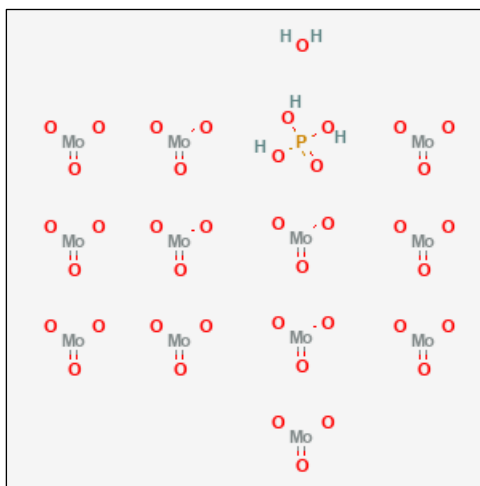

Figure 3.12: Phosphomolybdic acid (PMA) structure.

L-Cysteine

The L-Cysteine (121.1 g/mol) is an amino acid containing sulphur, it is versatile and used in many branches as medical, food industry and cosmetic (**figure 3.13**)
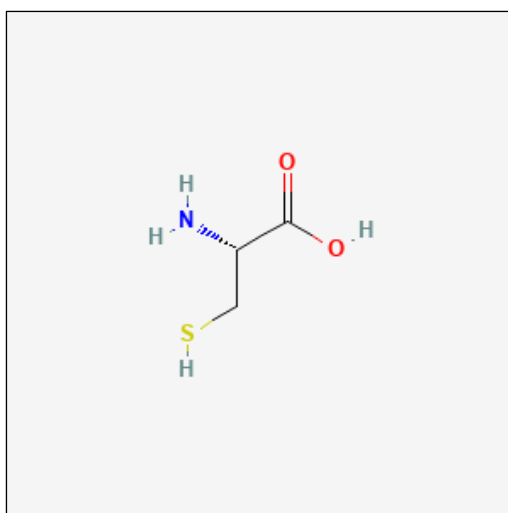

Figure 3.13: L-Cysteine structure.

Phosphate Buffer

(0.2M): NaH$_2$PO$_4$ (119.98 g/mol) - Na$_2$HPO$_4$ (141.96 g/mol)

Used to keep the pH of the reagents solution stable at 6.8 pH.

Hydroxypropyl Cellulose (HPC)

The HPC is a derivate of cellulose, a natural polymer derived from plant cell walls, and it is widely used in pharmaceuticals, food, and industrial applications due to its versatile properties (**figure 3.14**). HPC is a white to off-white, odourless powder that is soluble in both water and some organic solvents, making it unique among cellulose derivatives. HPC is non-toxic and biocompatible, its main applications are in pharmaceuticals, food industry and cosmetics. In this work was used as binder.
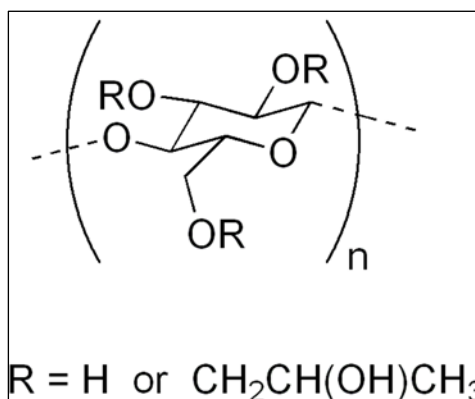
Figure 3.14: Hydroxypropyl Cellulose (HPC) structure.

Carboxymethyl Cellulose (CMC)

CMC is a widely used binder in various applications, particularly in the fabrication of electrodes for lithium-ion batteries and other electrochemical systems (**figure 3.15**). Its properties make it an effective choice for binding active materials, conductive additives, and current collectors in a slurry. It is water soluble making its application environmentally friendly by removing the need of toxic solvents to solubilize binders such as PVDF. It provides good mechanical stability, flexibility and it is inexpensive compared to other synthetic binders.
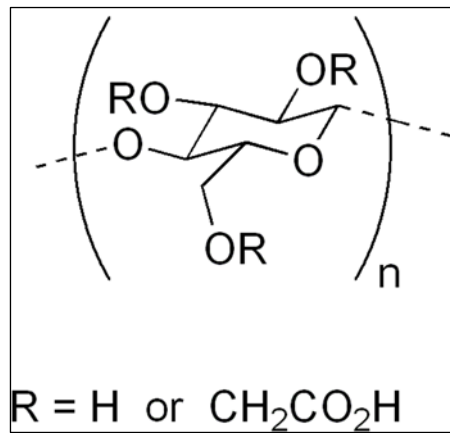
Figure 3.15: Carboxymethyl Cellulose (CMC) structure

1-Butyl-3-methylimidazolium tetrafluoroborate (BMIM BF4)

Is a widely studied ionic liquid used as an electrolyte in batteries and supercapacitors due to its wide electrochemical stability window and ionic conductivity (**figure 3.16**).
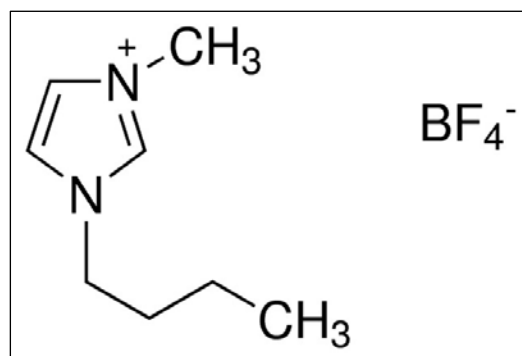
Figure 3.16: Molecule of BMIM BF_4

Graphene Oxide (GO) gel (2%wt)

The most studied material for 2D membranes is GO because it has a good tendency to create a compact structure and so a free-standing membrane (**figure 3.17**). It has been used in this study as a substitute for the binder, the advantage is that the GO also is a 2D material as MoS_2, but the disadvantage is that it is less environment friendly than binders like cellulose and that it is a poor electronic conductor.
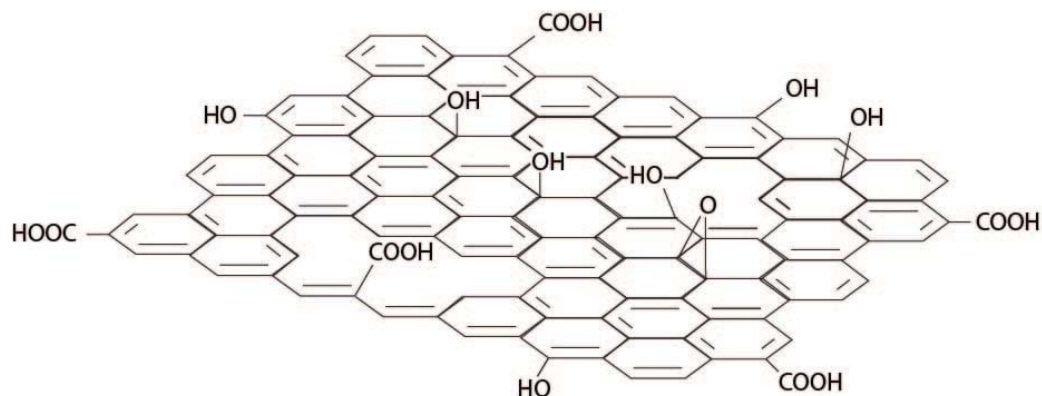
Figure 3.17: typical structure of a single layer graphene oxide with its typical functional groups.

Polyvinylidene fluoride (PVDF)

Polyvinylidene fluoride (PVDF) is a high-performance polymer known for its unique combination of chemical stability, mechanical strength, and piezoelectric properties (**figure 3.18**). It is widely used across various industries, particularly in energy storage, coatings, membranes and electronics. PVDF is widely used as a binder in the electrodes of lithium-ion batteries. It helps to hold active materials and conductive additives together, providing stability and flexibility to the electrode structure. Its electrochemical stability and strong adhesion properties contribute to battery performance and lifespan. Since PVDF is not soluble in water it is usually dissolved in NMP (N-methyl-2-pyrrolidone) a toxic solvent for the human and the environment, but in this work, it was dissolved in DMSO.
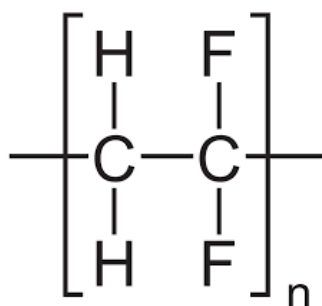
Figure 3.18: molecular structure of the PVDF polymer.

Dimethyl sulfoxide (DMSO)

Dimethyl sulfoxide (DMSO) is an organic solvent with the chemical formula $(CH_3)_2SO$ (**figure 3.19**). It is known for its versatility in both laboratory and industrial applications due to its unique properties, including high polarity, the ability to dissolve a wide range of substances, and its biological compatibility. DMSO is relatively safe to handle at low concentrations, and it is biocompatible, which has led to its use in pharmaceutical formulations and cell

cryopreservation. However, DMSO readily penetrates the skin, so caution is necessary as it can also carry other substances through the skin.
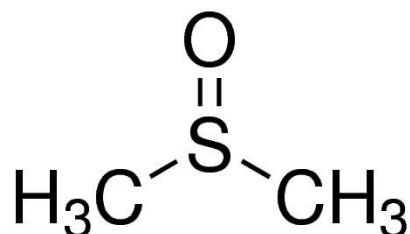
Figure 3.19: chemical structure of the DMSO.

Filters for vacuum filtration

Filters of different materials and porosity were used to support the filtration of the membranes:

- Alumina 0.2µm and 0.02µm porosity and 47mm diameter (Whatman Anodisc^{TM} 47).
- PES 0.2µm and 0.45µm porosity, cut into the required dimensions.
- Polycarbonate 0.1µm porosity and 47mm diameter.
- PTFE 0.1µm porosity and 47mm diameter.
- PC/PE 0.05µm porosity and 47mm diameter.

3.2 Synthesis and Preparation of Materials

3.2.1 Synthesis

Muffle hydrothermal synthesis

The MoS$_2$ was synthesized by hydrothermal synthesis inside two Teflon reactors of 25mL contained in the stainless-steel autoclaves. To prepare the 18mL solution of the reagents, 107mg of L-Cysteine and 106mg of PMA were mixed in distilled water, the pH of the solution was adjusted to 6.8 adding a phosphate buffer: (per 100mL) 0.1277 mol of Acid – 0.0722 mol of Base. The solution was sonicated to ensure the complete dissolution of the reagents and the buffer. Then, after pouring the solution of the reagents inside the Teflon reactors, the autoclaves were closed and placed in the muffle for 12h at 180°C, with an initial temperature ramp from 0°C to 180°C in 1h15min.

Once the hydrothermal synthesis is finished, the material is taken and placed in a falcon tube and then three washes with a centrifuge for 1h30min at 4000rpm were performed. At the end of each centrifuge the liquid is removed with a pipette and replaced with distilled water (see **figure x**).

At the end of the washes, the liquid is removed with a pipette, leaving the MoS$_2$ damp. The dump was frosted and then the lyophilizing process was held at −55 °C under vacuum (~3 × 10^{-3} mbar) for one week.

Microwave-assisted hydrothermal synthesis

To synthetize the MoS$_2$ with the microwave-assisted hydrothermal synthesis, the same solution of reagents and buffer was prepared, then placed inside the Teflon reactor of 50mL. Different tests were made changing the parameters (Temperature and time) and after the synthesis, the dispersion was washed with a centrifuge for 1h30min at 4000rpm for three times same as in the muffle method. **table 4.1** in the results chapter shows the attempts to produce MoS$_2$ from microwave assisted hydrothermal synthesis.

3.2.2 Membrane's Production

Vacuum filtration system

The membrane production was done by the vacuum filtration, the set-up is simple and usually more convenient for membranes than other techniques like dip coating, spray coating and spin coating because the filtration allow the flakes of 2D material to stack on top of each other creating a structure of nanochannels while removing most the water or other solvent, making the drying of the membrane quicker. The MoS$_2$ flakes interact only with Van der Waals forces, weaker forces than the hydrogen bonds in GO even though the distance between the flakes is lower. The 1T-MoS$_2$ is hydrophilic, and this may be a problem below the nanometer scale because hydrophilic solvation effects become significant, negatively affecting the sedimentation of flakes (the separation of flakes ranges from 0.3 to 0.9 nm) (**figure 3.20**).
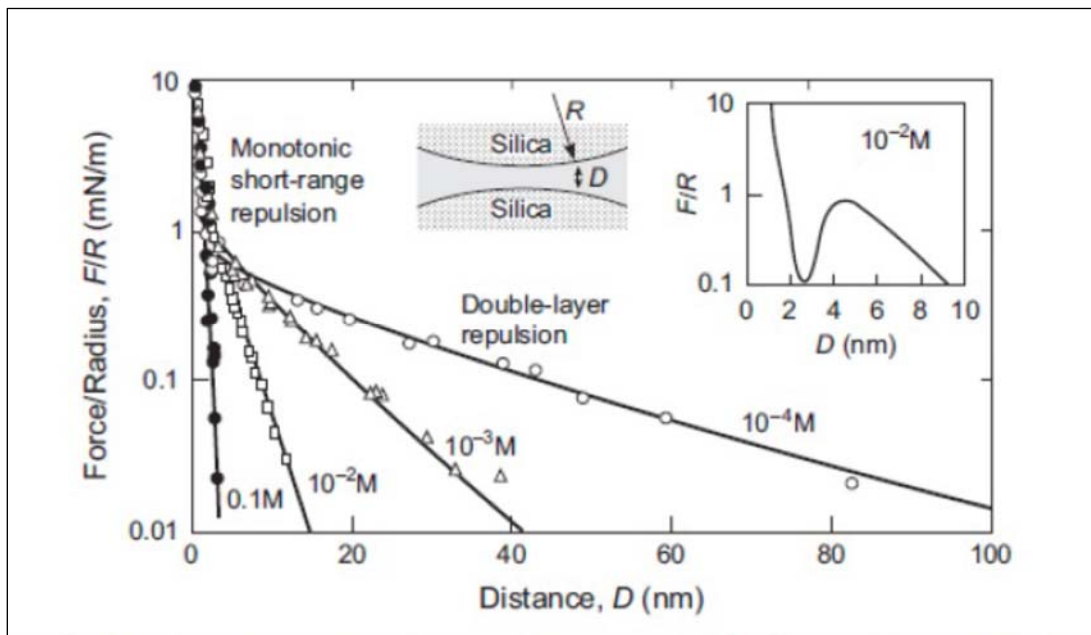
Figure 3.20: Repulsion of two silica particles as a function of distance from each other.

Doctor Blade

The production of a membrane or electrode with doctor blade was problematic due to the difficulty on separating the material from the substrate (glass or aluminium) and due to the slow evaporation of the DMSO, therefore this technique was not fully exploited.

3.3 Physical-Chemical Characterization Techniques

3.3.1 X-ray Diffraction (XRD)

X-ray Diffraction (XRD) is a powerful analytical technique used to study the crystalline structure of materials. It provides detailed information about the atomic arrangement, crystallinity, phase identification, and crystal orientation of a sample. XRD is widely used in fields such as materials science, chemistry, mineralogy, and physics to characterize the structure of a variety of solid materials.

X-ray diffraction relies on the fact that when a material is exposed to X-rays, the X-rays interact with the crystalline lattice of the material. If the material is crystalline, the lattice acts like a diffraction grating, and the X-rays are scattered in specific directions according to the Bragg's Law:

$$n\lambda = 2d\sin\theta \qquad (1)$$

Where:

- n = an integer (the order of diffraction),
- λ = the wavelength of the X-rays,
- d = the spacing between planes in the crystalline lattice,
- θ = the angle of incidence of the X-ray beam (Bragg angle).

When the angle of incidence is such that the condition of Bragg's Law is met, constructive interference occurs, and a diffraction peak is produced, which can be measured and analysed (**figure 3.21**).

Figure 3.21: Bragg's Law condition of constructive interference between the paths ABC and A'B'C' [87].
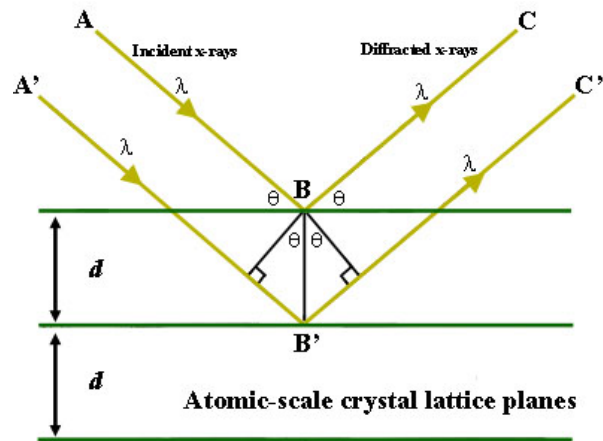
The XRD patterns were collected using an X-Ray diffractometer (Empyrean, Anton Paar) with CuKα radiation (λ = 1.54059 Å) at 40 kV, and 40 mA, and a 0.026 step size. The goal was to study the characteristic peaks to measure the interlayer distance between the flakes of GO and MoS_2.

3.3.2 Field Effect Scanning Electron Microscopy (FESEM)

FESEM stands for Field Emission Scanning Electron Microscopy, a type of scanning electron microscope (SEM) that uses a field emission gun (FEG) as the electron source (**figure 3.22**). FESEM is a powerful imaging technique that provides detailed, high-resolution images of surfaces, materials, and structures at the nanometer and even atomic scale.

FESEM uses a field emission gun instead of the conventional thermionic electron gun found in traditional SEM. The FEG generates electrons by applying a high electric field to a sharp metal tip, which causes electrons to be emitted from the tip even at low temperatures. This provides higher brightness and lower energy spread than thermionic guns, resulting in improved resolution and contrast in the images.

The instrument can achieve higher resolution imaging (typically 1–2 nm) compared to conventional SEM, allowing it to capture finer details of the sample's surface. This makes it ideal for studying nanomaterials, thin films, and other structures at a very high magnification. The field emission gun produces a narrower electron beam with higher current density, which enhances the signal-to-noise ratio and provides clearer and more detailed images, even at high magnifications.

FESEM uses secondary electrons (SE) and backscattered electrons (BSE) to create images: Secondary electrons (SE) provide surface detail and topographical contrast. Backscattered

electrons (BSE) provide elemental contrast because the intensity of BSE depends on the atomic number (Z) of the elements in the sample.

One of the key advantages of FESEM is its ability to generate high-resolution 3D images of the surface structure of a material. This is due to the high angular resolution of the electron beam and the detector system.
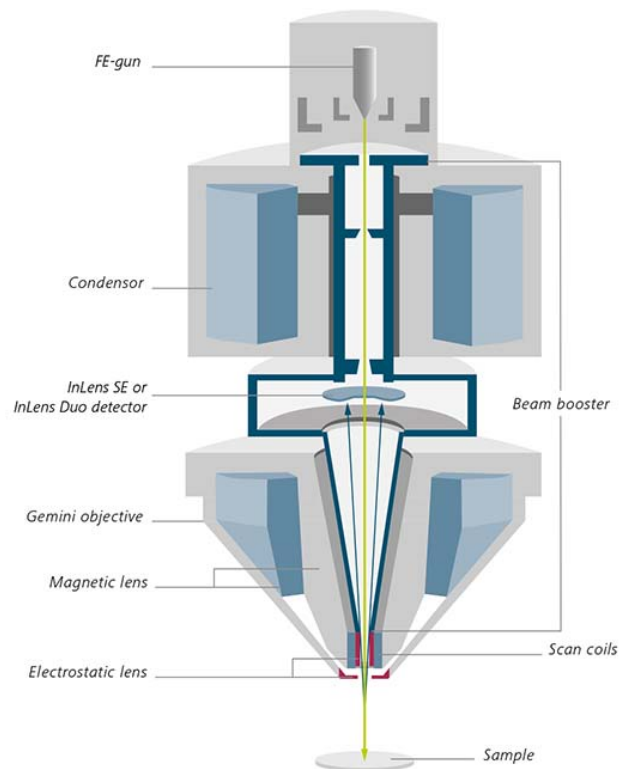
Figure 3.22: scheme of a FESEM with its components [100].

The FESEM was used in conjunction with an Energy Dispersive X-ray Spectroscopy (EDS) analyser to provide elemental analysis of the sample's composition. EDS works by detecting X-rays that are emitted from the surface of a sample when it is bombarded with an electron beam in the SEM. When the electron beam interacts with the sample, it causes the elements in the sample to emit secondary X-rays characteristic of their atomic structure. These X-rays are then detected and analysed by the EDS system to determine the elemental composition of the sample.

The ZEISS Supra 40 Field Emission Scanning Electron Microscopy (**figure 3.23**) was used to study the topology of the membrane (MoS$_2$/GO) in cross section and from above, the MoS$_2$ powder and to map the elements and the Secondary Electron images were captured with an in-lens detector. The in-lens detector is a specialized type of electron detector positioned within

the column of the microscope, often near the objective lens or integrated with them. The primary purpose of an in-lens detector is to collect electrons with high efficiency ideal to give high-resolution image of nanoscale materials.

Figure 3.23: The FESEM set up in the laboratory.

3.4 Electrochemical Characterization Techniques

3.4.1 Electrochemical Impedance Spectroscopy (EIS)

Electrochemical Impedance Spectroscopy (EIS) is a powerful analytical technique used to study the electrical properties of materials and interfaces in electrochemical systems. It provides information about the dynamics of processes such as charge transfer, mass transport, and capacitance by applying a small alternating signal to the system and measuring the resulting impedance over a range of frequencies.

Impedance represents the ability to resist the passage of a current and can be obtained by applying an alternating potential to the cell and measuring its response in alternating current. If the potential oscillations are small, the response current oscillates at the same frequency as the potential, but it presents a phase deviation. Under these conditions, it is possible to derive the impedance using Ohm's law, by relating potential and current:

$$Z = \frac{V}{I} = \frac{V_0 \sin \omega t}{I_0 \sin(\omega t + \rho)} = Z_0 \frac{\sin \omega t}{\sin(\omega t + \rho)} \tag{2}$$

where:

- V is the potential
- Z is the impedance
- V_0 is the max amplitude of the voltage

- I_0 is the max amplitude of the current
- t is the time
- Z_0 is the max amplitude of the impedance
- I is the response current
- ω is the oscillation frequency
- φ is the phase deviation

The most common plots for EIS are the Nyquist plot and the Bode plot. In the first the imaginary part of the impedance (-Z'') and the real part (Z') are plotted to visualize the resistive, inductive or capacitive behaviour of a system at different frequencies. The latter is a graphical representation of a system's frequency response representing in two separate plots the magnitude (dB) and the degrees (°) versus the frequency. Phase plot measures the phase shift introduced into the system, expressed in degrees at the frequency where gain equals 0 dB. Magnitude plot, on the other hand, is measured at the frequency where the phase shift equals -180° and it represents the gain (amplification or attenuation) of the signal.

3.4.2 Linear Sweep Voltammetry (LSV) and Cyclic Voltammetry (CV)

Voltammetries are electrochemical techniques used to study the redox (oxidation-reduction) behaviour of chemical species and to gain insights into reaction kinetics, thermodynamics, and mechanisms. It is one of the most common methods in electrochemistry because it provides detailed information such as the values of potentials at which oxidation and reduction reactions occur, how reversible they are and how they are affected by the scanning speed.

In a voltammetric experiment a voltage sweep is set, this is the potential (Volts) applied to the working electrode, and it is linearly swept over a defined range (linear sweep voltammetry, LSV) and then reversed, forming a cycle (cyclic voltammetry, CV). As the potential changes, the current response is measured, and it depends on the electrochemical reaction taking place at the working electrode. The result is plotted as a voltammogram, a plot of current (y-axis) versus applied potential (x-axis), which shows the characteristic "fingerprints" that correspond to oxidation and reduction reactions or other kind of behaviour such as intercalation and electrical double layer.

The key parameters in Cyclic Voltammetry are:

- Scan Rate: The rate at which the potential is swept (e.g., mV/s). The scan rate affects the peak shapes and positions and provides information about reaction kinetics.

- Peak Potential: The potential at which the maximum current occurs during oxidation (anodic peak) or reduction (cathodic peak).

- Peak Current: The maximum current observed at each peak. This is related to the concentration of the electroactive species and the electron transfer rate.

- Reversibility: In reversible systems, the anodic and cathodic peaks are well-defined and symmetrical, and the peak separation can help determine the number of electrons involved. Irreversible or quasi-reversible systems display distorted or shifted peaks while for a reversible system, the peak separation between the anodic and cathodic peaks is around 59.2 mV (for one-electron reactions at room temperature). Larger separations indicate slower electron transfer or irreversible processes.

The main information obtained from CV are:

- Redox Potentials: CV helps determine the formal potential of redox reactions.

- Reaction Mechanisms: By analysing the shape, position, and relative height of peaks, researchers can gain insights into complex electrochemical mechanisms, including multi-electron transfers or coupled chemical reactions.

- Kinetics: The current response and peak shapes give information about the electron transfer rate and diffusion of the species to the electrode.

- Diffusion Coefficients: Using the Randles–Sevcik equation, the diffusion coefficient of the analyte can be estimated from the peak current.

In energy storage, the CV figures are indicative on the interaction between the electrolyte and the electrodes: double layer capacitance is described by squared box-like rectangular voltammogram, the same shape but with higher current density belongs to pseudocapacitance dominated by surface redox reactions. Instead, if the redox reactions are not limited to the surface, the reactions occur at a specific voltage, generating two distinct peaks (anodic and cathodic) characteristic of materials employed in batteries (**figure 3.24**). Pseudocapacitors in which the charge storage is dominated by redox reactions and intercalation show two peaks that are almost reversible (peak separation) and with large FWHM, therefore the energy (voltage) of the reaction is spread and less distinct (as in batteries).

When dealing with capacitive materials, the metrics matter. For purely EDLC electrodes and devices, the "capacitance" can be reported in Farad (F/g or F/cm2 or F/cm3), while when dealing with pseudocapacitance or hybrid devices it is recommended to use "capacity" in Ampere per hour (mAh/g, ecc).

Those values can be retreived from the CV graphs were calculated using the following equation for asymmetric cells [88]:

$$C_s = \frac{1}{2mv\Delta V} \int_{V_0}^{V_1} I(V)dV \qquad (3)$$

Where C_s is the capacitance, m is the mass of the electrode, v is the scan rate ΔV is the potential window of the CV analysis, I is the current response.

To convert the capacitance into capacity the C_s value was multiplied by the potential window ΔV and divided by the 3.6 to obtain mAh/g.

In case of pure EDLC or for perfect capacitive-controlled mechanism in pseudocapacitor materials, the equation highlights the fact that the capacitance is independent with respect to the scan rate:

$$C = q/\Delta V \qquad\qquad (4)$$
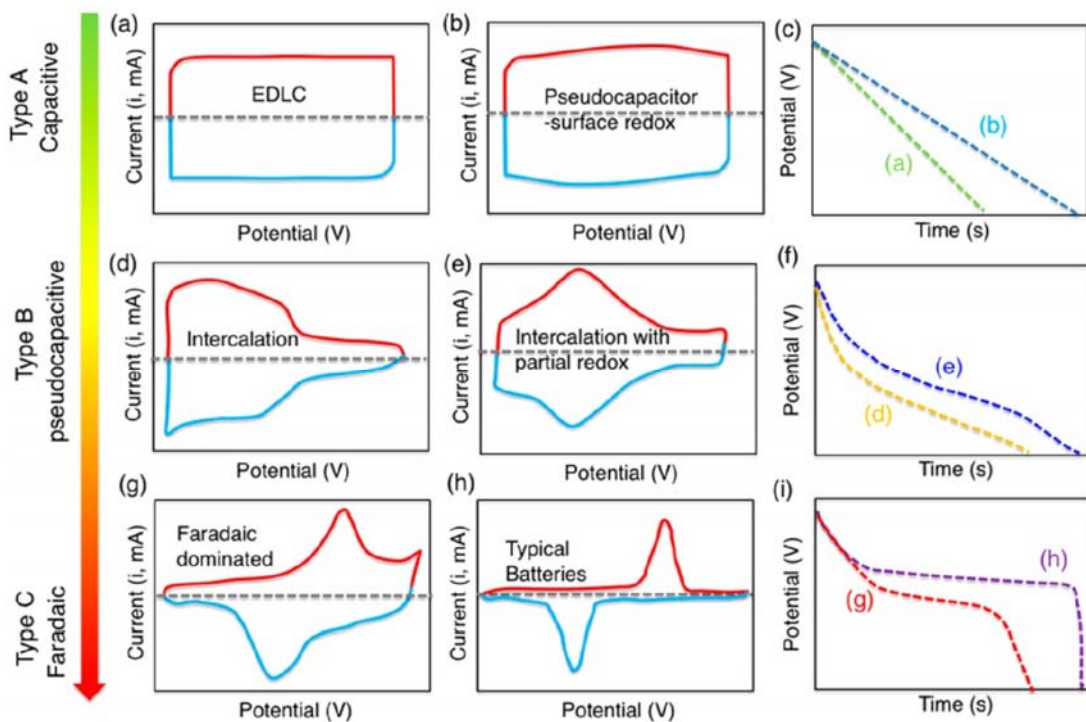
Figure 3.24: Examples of different storage mechanisms identified by their voltammograms (a,b,d,e,g,h) and their galvanostatic profiles (c,f,i) [49].

But not all the materials show such behaviour, in fact it is common to observe in cyclic voltammetry that by normalizing the current with respect to the scan rate and plot is vs the potential or voltage window, the datapoints are not overlapped, meaning that there is a time dependence on the storage capacity of the material.

In order to understand if the material stores charges by means of capacitive-controlled processes or by diffusion-controlled processes typical of battery materials, half-cells in 1 M LiPF6 in EC:DMC vs. Li were characterized.

The coin cells were prepared inside the glove box after drying the working electrode and glass microfibre separator (Whatman® Grade GF/D, with a thickness of 675 μm and diameter of 18mm) at 80°C for one night inside the Buchi oven under vacuum. Inside the glovebox filled with Argon, the coincells where then assembled as illustrated in **figure 3.25**.

At the working electrode, the material under test was placed, separated by the counter electrode of metallic lithium by means of a glass-fiber membrane (CODE). Two types of working electrodes were evaluated:

1. Standard electrodes made with 70% MoS_2, 20% of carbon black (MTI) and 10% of polyacrylic acid solution (Sigma-Aldrich) over a carbon-coated aluminium current collector. Electrodes of 15 mm of diameter were obtained with an average mass of 8.5 mg in which the active material (MoS_2) was of 0.56 mg.
2. Membrane of MoS_2/GO (19) made with 20mg MoS_2 and 10mg GO. The membrane was cut in 15 mm diameter disks with an average mass of 2.3 mg in which the active material (MoS_2) was of 1.53 mg.

Coin cells were cycled between 1 to 3 V vs. Li/Li+ at different scan rates starting from 0.1 mV/s in order to allow the cell to mature the SEI in the first cycle. 0.1 mV/s was performed for 5 cycles, the following cycles up to 2 mV/s were performed 3 times per scan rate.
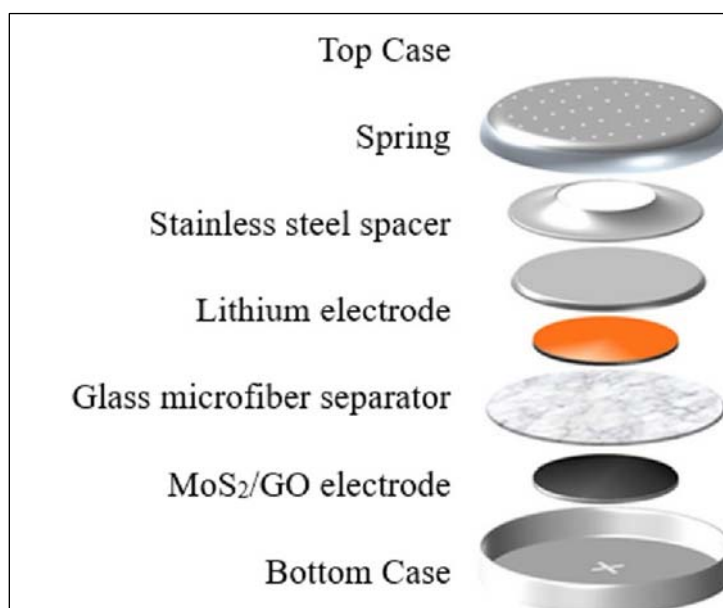

Figure 3.25: example of assembled coincell.

The analysis based on the scan rates was done in order to perform a kinetic analysis. The kinetic analysis is useful to separate the diffusion-controlled current to the capacitive-controlled current, this allows us to quantify the diffusive and capacitive contribute to the reactions in the

cells by analysing how the current varies with the frequency. The next paragraph will explain how this method morks.

Trasatti et al. [89] proposed a distinction between "outer" surface redox contributions and "inner" redox contributions. They suggested that the outer surface charge (q_o) is independent of the scan rate (v), while the total charge (q_t) within the bulk of the electrode varies linearly with the square root of the scan rate ($v^{-1/2}$).

Additionally, Conway et al. [90] investigated electrochemical processes by analysing how the peak current (i_P) changes with the potential sweep rate (v): i_P increases linearly with v for surface-controlled processes, whereas it varies with $v^{1/2}$ for diffusion-controlled processes.

Dunn et al. [90] extended Conway's approach by introducing a method to deconvolute the current into surface capacitive contributions (which change linearly with v) and diffusion-controlled intercalation processes (which vary with $v^{1/2}$) at any given potential (V). This led to the formulation of the following equations:

$$i(V) = k_1 v + k_2 v^{1/2} \tag{4}$$

$$\frac{i(V)}{v^{1/2}} = k_1 v^{1/2} + k_2 \tag{5}$$

Where k_1 and k_2 are the two potential dependant constants corresponding to the capacitive and diffusion-controlled contribution, i is the current (A/cm^2) and v the potential scan rate (V/s). These equations can be used to evaluate the kinetics of the energy storage.

Dunn method doesn't take into account shifts of the peak potential due to polarization processes, another simple method could be Specs and MUSCA (**figure 3.26**) they both take into account a third component that is called "residual" in which falls multiple contributions.

Step potential electrochemical spectroscopy (SPECS), was developed by Donne et al. [91] to reconstruct the voltammograms by deconvoluting the current ($i_{overall}$) with a linear combination of its contributes capacitive (i_C), diffusion-controlled (i_D), and residual (i_R) currents:

$$i_{overall} = i_C + i_D + i_R \tag{6}$$

SPECS experiment consist in an electrochemical spectroscopy, where a series of small potential steps are applied giving enough time between them to allow the electrode to reach a quasi-equilibrium measuring the current flow as a function of time.

Multiple-step chronoamperometry (MUSCA) developed by Shao et al. [90], is a method developed to minimize the the ohmnic drop contribution by holding each potential enough time to reach equilibrium at the steady-state current. Allowing to reconstruct the voltammorgams mitigating the impact of the ohmnic drop.
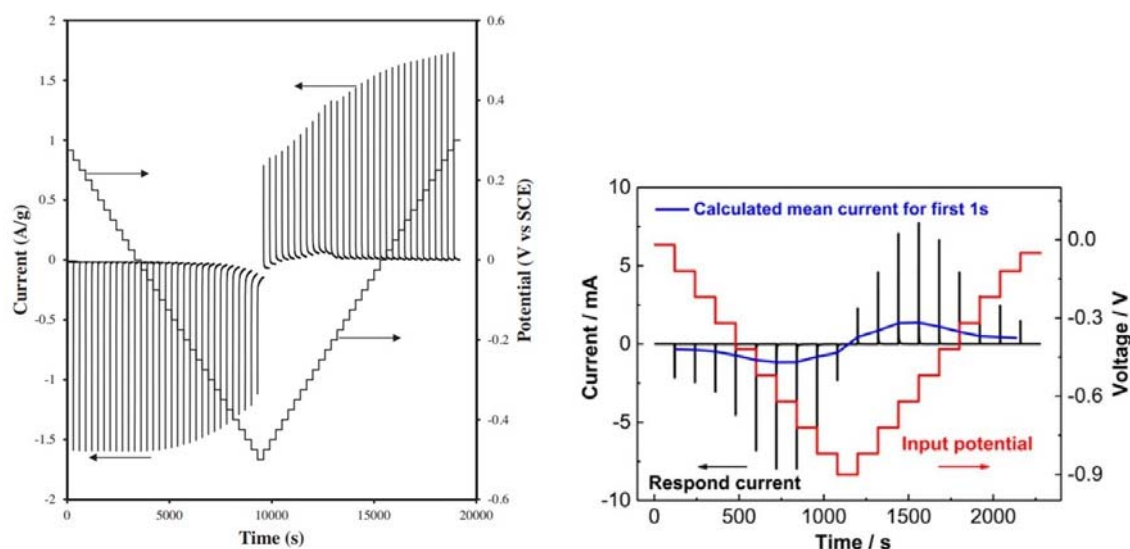
Figure 3.26: exhample of data set for SPECS and MUSCA [90,91].

3.4.3 Permselectivity

Permselectivity refers to the selective permeability of a membrane or barrier to different substances. It is a property that describes how a membrane allows certain particles, ions, or molecules to pass through while blocking others. This selective nature is often based on size, charge, or chemical affinity. The permselectivity of a membrane is an important aspect for the development of storage device like redox flow batteries (RFBs), but also for applications as the recovery of ions as Lithium to mitigate the supply shortages, it scales from 0 to 1 where 1 means perfect selectivity of the counterions. Membranes can be selective towards cations, named cation exchange membranes (CEMs) or selective towards anions and called anion exchange membranes (AEMs), the surface charge of the membrane will be determining on the ion to which it is selective attracting ion of the opposite charge of the membrane surface.

The setup used for the measurement is a two-compartment diffusion cell in a two-electrode system, the Ag/AgCl electrodes were used as reference electrode (RE) and secondary electrode (SE). The permselectivity measurement requires a gradient in concentration, one cell was filled with a 0.5M solution and the other one with a 0.1M solution for all the three electrolytes (NaCl, KCl and LiCl) (**figure 3.27**).
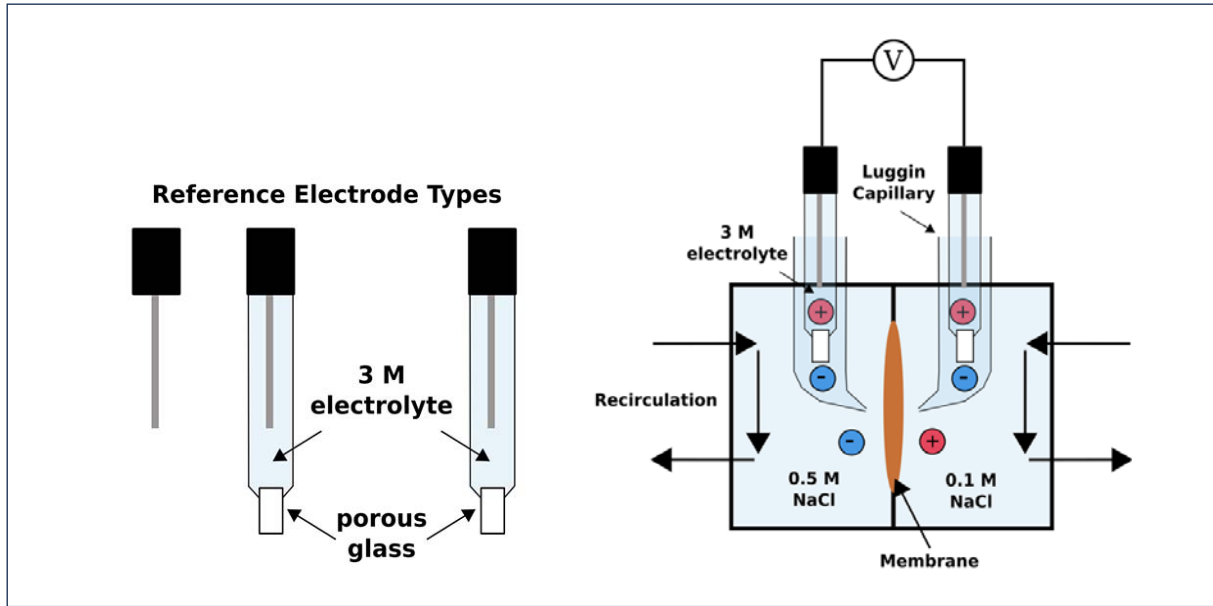
Figure 3.27: (a) RE and SE made of Ag/AgCl in 3 M KCl, (b) scheme of the setup for the permselectivity measurment [92].

The apparent permselectivity of the membrane can be calculated using E_{mem} the potential across the membrane, E_{the} the potential of an ideal membrane obtained from the Nernst equation (4), t_g and t_c respectively the transport numbers of counterions and co-ions, a_i is the mean activity of the salt, $\gamma_\pm$ is the activity coefficient, $m_\pm$ is the molality, μ_i is the mobility of the ion. The following equations were used to calculate the permlesectivity [92,93,94]:

$$\alpha_{ap} = \frac{E_{mem}}{E_{the}} \tag{7}$$

$$\alpha_{tn} = \frac{\frac{E_{mem}}{E_{the}} + 1 - 2t_g}{2t_c} \tag{8}$$

$$E_{mem} = E_{meas} - \Delta E_{offset} - \Delta E_j \tag{9}$$

$$E_{the} = -\frac{RT}{z_i F} \ln \frac{a_{\pm 0.5}}{a_{\pm 0.1}} \tag{10}$$

$$E_j = \frac{\sum_i^n \frac{|z_i|\mu_i}{z_i}[a_i(2) - a_i(1)]}{\sum_i^n |z_i|\mu_i[a_i(2) - a_i(1)]} \frac{RT}{F} \ln \frac{\sum_i^n |z_i|\mu_i a_i(1)}{\sum_i^n |z_i|\mu_i a_i(2)} \tag{11}$$

$$a_\pm = \gamma_\pm m_\pm \tag{12}$$

- $|z_i|$ is the module of the charge of the counterion (the ion with opposite charge to the membrane) and it's always equal to 1 with the electrolytes used.
- $a_\pm$ is the mean activity of the salt

40

- E_j is the junction potential
- E_{the} is the potential of an ideal membrane calculated with the Nerst equation
- E_{mem} is the potential across the membrane
- α_{tn} is the apparent permselectivity
- α_{ap} is the permselectivity taking into account the transport numbers of the ions

To obtain the the mean ion activity the equation (12) is used. Abbas et al. [95] was employed for the mean ionic activity coefficients $\gamma_\pm$, the values are represented in **table 3.1** together with the other parameters.

(F=96485 Cmol^{-1}, R=8.314 Jmol^{-1}K^{-1}, T=296.15 K)

Table 3.1: parameters for the three different electrolytes [94]

	$\gamma_{0.5}$	$\gamma_{0.1}$	E_{the}	t_g	t_c	$E_{j,conc}$	$E_{j,dil}$	ΔE_j
KCl	0.649	0.768	-36.99 mV	0.491	0.509	0.89	1.69	-0.80
NaCl	0.679	0.777	-37.86 mV	0.396	0.604	-0.59	1.27	-1.85
LiCl	0.739	0.789	-39.64 mV	0.336	0.664	-1.37	1.06	-2.43

The solution used are NaCl, KCl and LiCl, concentrations were 0.1M and 0.5M on the two cells for all the three solutions. E_{offset} was measured with both electrodes into the solution, first 0.5M than 0.1M and took the values as the average.

3.4.4 Ionic Resistance

The ionic resistance (Ω) refers to the resistance encountered by ions as they move through a medium, such as a liquid electrolyte, solid electrolyte, or other ionic conductor. This resistance plays a critical role in systems like batteries, fuel cells, electrochemical sensors, and capacitors and it depends on mobility of the ions in the membrane which depends strongly on the nature of the mobile ion species: valence, size, hydration.

The set up is similar to the permselectivity but with four electrodes where working electrode (WE) and counter electrode (CE) are titanium grids with inside active carbon electrode, secondary electrode (SE) and reference electrode (RE) are the Ag/AgCl immersed in KCl 3M (**figure 3.28**). The SE and RE always measure voltage while WE and CE the current. The diameter of the cell hole-compartment for the membrane is 14.5mm with an area of 1.65cm^2.
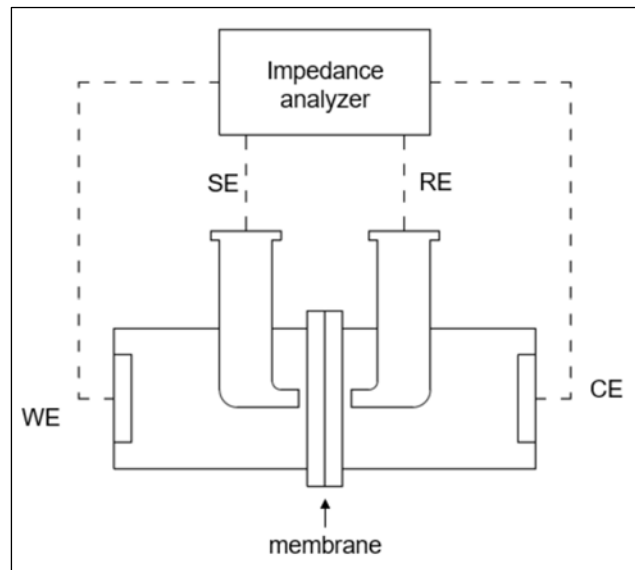
Figure 3.28: Scheme of the experimental set up to measure the ionic resistance of the membranes [94].

There are three ways to measure the ionic resistance of a membrane [96]:

- IES: It measures with alternate current (AC) the impedance of the system, the resistance is measured on the x-axis where the imaginary values (y-axis) go to zero, (**figure 3.29**).
- Linear sweep voltammetry potentiostatic: the potential at the electrodes is swept while the current is measured. The resistance is the slope of the curve (**figure 3.30**), obtained from the Ohm law (VR=I) where V is the potential, I the current and R the resistance.
- Linear sweep voltammetry galvanostatic: The current at the electrodes is swept while the voltage is measured. The resistance is the slope of the curve, same as linear sweep potentiostatic.

For every electrolyte it was performed a resistivity measurement without the membrane, the results must be subtracted from the membrane measurements to obtain the membrane resistivity. The resistance of the membrane was calculated following the equation:

$$R_m = R_{measured} - R_{blank} \qquad (13)$$

Where R_{blank} is the resistance of the electrolyte, $R_{measured}$ is the resistance measured with the membrane and R_m is the resistance of the membrane that was than multiplied by the area of the exposed membrane.

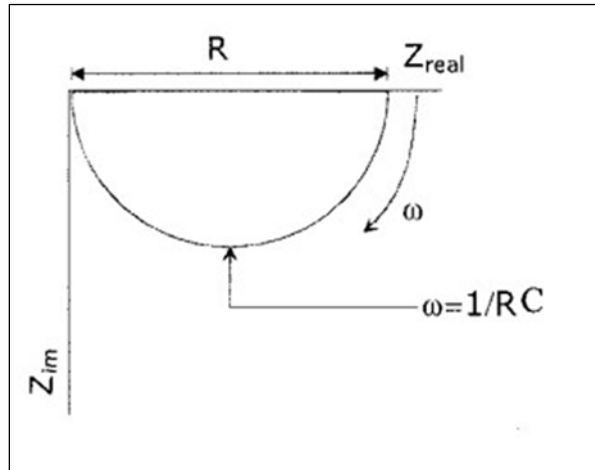**Figure 3.29**: Results of an impedance spectroscopy of a system with capacitance (Z_{im}) and resistance Z_{real}) in parallel. The imaginary values go to zero at really low frequencies [96].
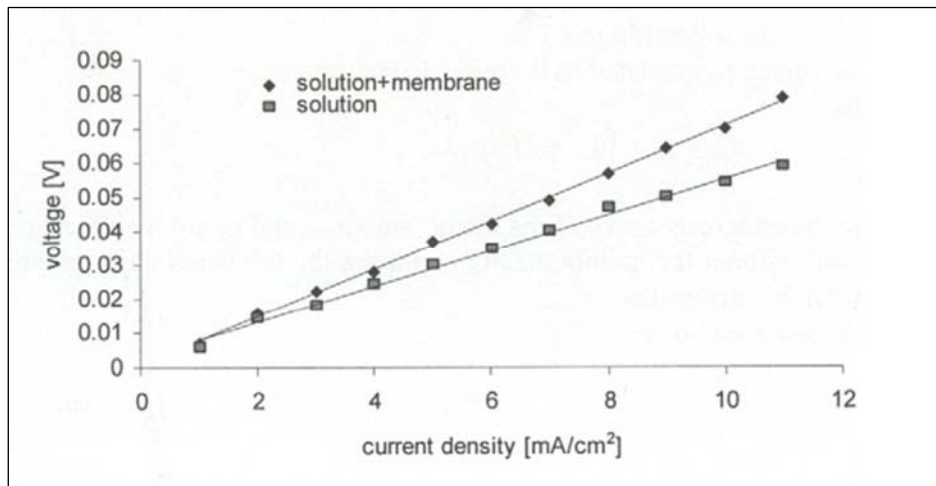

Figure 3.30: results of a DC measurment, showing the voltage drop as a funcion of the current density [96].

EXPERIMENTAL RESULTS

4.1 Synthesis of MoS$_2$

Muffle

The MoS$_2$ was synthesized via hydrothermal synthesis using two Teflon-lined reactors (25 mL capacity) placed inside stainless-steel autoclaves. For the preparation of 18 mL reagent solution, 107 mg of L-cysteine and 106 mg of PMA were dissolved in distilled water. The pH of the solution was adjusted to 6.8 using a phosphate buffer prepared with 0.1277 mol of acid and 0.0722 mol of base per 100 mL.

The production of the material was of laboratory scale because of the volume of the two small Teflon reactors filled with only 18mL of reagents and because of the yield of hydrothermal synthesis which was only about 60% (**figure 4.1**). The yield was calculated by weighting the dry MoS$_2$ powder for one the single synthesis and divided it by the weight of the Mo and S in the reagents.
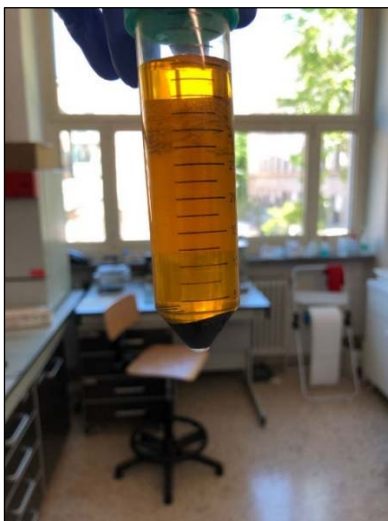
Figure 4.1: MoS$_2$ synthesized in a muffle after the first centrifuge.

Microwave

The microwave-assisted hydrothermal synthesis was carried out with the aim to decrease the time of the synthesis itself and to produce more active material being the reactor of 50 mL of volume. Among the possible synthetic parameters, the temperature couldn't be increased because of the limit of the Teflon autoclave suggested by supplier that was already around 180°C, therefore the time of the reaction was progressively increased from 30min to 4h30min. It has been observed that the use of the microwave does not speed up the synthesis as in the literature [64-76] (**figure 4.2 left**). Actually, there are no studies that show the use of microwave

with the same reagents that we used in the tests. Only the test number 6 was successful (**figure 4.2 right)**, and we observed the production of solid material. The mass produced in the test number 6 (**table 4.1**) is equivalent to the standard oven hydrothermal synthesis.

Table 4.1: microwave-assisted synthesis with their parameters.

	Ramp	Temperature	time
1	5min	180°C	30min
2	5min	180°C	1h
3	5min	190°C	30min
4	5min	180°C	1h30min
5	5min	180°C	3h
6	5min	180°C	4h30min

Figure 4.2: Microwave-assisted synthesis 1 (left) and 6 (right).

The solvent used to perform the microwave-assisted hydrothermal synthesis is water, but there are other polar solvents with higher efficiency that could help improving the effectiveness of the microwave absorption. Water is a solvent with high dielectric constant (ε) equal to 80.4, but the dielectric loss (ε'') is another parameter to keep an eye on when performing microwave synthesis and for water its value is 9.889 while there are many solvents with higher values as

ethylene glycol (49.950). While the dielectric constant measures the ability to store charge, the dielectric loss stays for how much of the input energy is lost and dissipated by heat. To take account of both the parameters it's used the following equation [97]:

$$tan\delta = \frac{\varepsilon''}{\varepsilon}$$ (14)

Where tanδ is the new parameter, ε and ε" are dielectric constant and dielectric loss. There also to consider the dependence to the temperature and the frequency to the dielectric constant, the result suggests many new solvents to replace the water (**figure 4.3**).

Solvent (bp °C)	Dielectric Constant (ε)	Solvent	Tan δ	Solvent	Dielectric Loss (ε'')
Water (100)	80.4	Ethylene Glycol	1.350	Ethylene Glycol	49.950
Formic Acid (100)	58.5	Ethanol	.941	Formic Acid	42.237
DMSO (189)	45.0	DMSO	.825	DMSO	37.125
DMF (153)	37.7	2-Propanol	.799	Ethanol	22.866
Acetonitrile (82)	37.5	1-Propanol	.757	Methanol	21.483
Ethylene Glycol (197)	37.0	Formic Acid	.722	Nitrobenzene	20.497
Nitromethane (101)	36.0	Methanol	.659	1-Propanol	15.216
Nitrobenzene (202)	34.8	Nitrobenzene	.589	2-Propanol	14.622
Methanol (65)	32.6	1-Butanol	.571	Water	9.889
NMP (215)	32.2	Isobutanol	.522	1-Butanol	9.764
Ethanol (78)	24.3	2-Butanol	.447	NMP	8.855
Acetone (56)	20.7	2-Methoxyethanol	.410	Isobutanol	8.248
1-Propanol (97)	20.1	o-Dichlorobenzene	.280	2-Butanol	7.063
MEK (80)	18.5	NMP	.275	2-Methoxyethanol	6.929
2-Propanol (82)	18.3	Acetic Acid	.174	DMF	6.070
1-Butanol (118)	17.1	DMF	.161	o-Dichlorobenzene	2.772
2-Methoxyethanol (124)	16.9	1,2-Dichloroethane	.127	Acetonitrile	2.325
2-Butanol (100)	15.8	Water	.123	Nitromethane	2.304
Isobutanol (108)	15.8	Chlorobenzene	.101	MEK	1.462
1,2-Dichloroethane (83)	10.4	Chloroform	.091	1,2-Dichloroethane	1.321
o-Dichlorobenzene (180)	9.9	MEK	.079	Acetone	1.118
Dichloromethane (40)	9.1	Nitromethane	.064	Acetic Acid	1.079
THF (66)	7.4	Acetonitrile	.062	Chloroform	0.437
Acetic Acid (113)	6.2	Ethyl Acetate	.059	Dichloromethane	0.382
Ethyl Acetate (77)	6.0	Acetone	.054	Ethyl Acetate	0.354
Chloroform (61)	4.8	THF	.047	THF	0.348
Chlorobenzene (132)	2.6	Dichloromethane	.042	Chlorobenzene	0.263
o-Xylene (144)	2.6	Toluene	.040	Toluene	0.096
Toluene (111)	2.4	Hexane	.020	o-Xylene	0.047
Hexane (69)	1.9	o-Xylene	.018	Hexane	0.038

Figure 4.3: dielectric constants and tan-delta for solvents applicable in microwave synthesis [97].

Unfortunately, the synthesis with new solvents couldn't be tested out due to a damage of the equipment that required longer time to fix than the time expected for the end of this thesis.

4.2 Membrane Fabrication

The membrane fabrication was performed with a vacuum filtration system, where different quantity of active materials and combinations with binders and filters were tested to obtain a self-standing membrane.

The following table (**Table 4.2**) represent some of the many attempts to produce a self-standing membrane.

Table 4.2: membranes produced by vacuum filtration with different methods and materials.

	MoS_2	Binder	Solvent	Filter	Duration
1	125mg	/	100ml DI-w	Alumina 0.2µm	30s
2	31mg	/	60mL DI-w	Alumina 0.2µm	Some second
3	31mg	3.2mg HPC	60mL DI-w	PC 0.1µm	30min
4	31mg	3.2mg HPC	60mL DI-w	Alumina 0.2µm	13min
5	31mg	3.2mg HPC	60mL DI-w	Alumina 0.2µm	13min
6	62mg	3.2mg HPC	120mL DI-w	Alumina 0.2µm	30min
7	31mg	1.55mg CMC	60mL DI-w	PC 0.1µm	2h
8	31mg	2mg CMC	60mL DI-w	Alumina 0.2µm	3min
9	31mg	3.11 CMC	60mL DI-w	PES 0.45µm	11min
10	31mg	4.65mg CMC	60mL DI-w	PC 0.1µm	1h35min
11	15mg	1.55mg CMC	60mL DI-w	PES 0.45µm on Alumina 0.2µm	5min
12	46.5mg	4.65mg CMC	93mL DI-w	PES 0.45µm on Alumina 0.2µm	45min
13	28mg	(added BMIM BF$_4$ later)	56mL DI-w	Alumina 0.2µm	30s
14	28mg	2.8mg CMC	112mL DI-w	PES 0.2µm	3h
15	14mg	2.4mg CMC	280mL DI-w	PC/PE filter 0.05um	night

16	14mg	2.4mg CMC	60mL DI-w	Alumina 0.02μm	night
17	20mg	/	10mL DMSO	Alumina 0.02μm	night
18	30mg	3mg PVDF	15mL DMSO	Alumina 0.02μm	night
19	20mg	10mg GO	10mL DMSO	Alumina 0.02μm	night
20	Double filtration: first 1mg GO than 20mg MoS$_2$				
21	20mg	5mg GO	10mL DMSO	Alumina 0.02μm	night
22	Only 10mg GO as reference membrane for characterizations				
23	20mg	5mg GO	10mL DMSO	Alumina 0.02μm	night
24	20mg/10mL DMSO + 2mg GO (double filtration, first GO than MoS$_2$)				
25	20mg	7mg GO	10mL DMSO	Alumina 0.02μm	night
26	20mg/10mL DMSO + 2mg PVDF + 2mg GO (double filtration, first GO than MoS$_2$ with PVDF)				
27	20mg/10mL DMSO + 2mg GO (double filtration, first GO than MoS$_2$)				
28	20mg	15mg GO	10mL DMSO	Alumina 0.02μm	night
29	15mg	10mg GO	7.5mL DMSO	Alumina 0.02μm	night

Problems encountered during the fabrication of such membranes are:

- Membranes 1 – 13: poorly diluted suspensions without binders could not remain stable, producing agglomerates during the magnetic stirring. If the duration of the filtration process exceeded tens of minutes, agglomerates are visible
- Membrane 3 – 4: The use of HPC as a binder was found to be incompatible (membrane 3,4) even worse than the membrane without binder (membrane 1 in **figure 4.5 a**), producing cracked and extremely fragile membranes.
- An attempt to produce a MoS$_2$ hydrogel membrane was made following Yayun et al. [98]. Right after the filtration, the wet membrane was immersed in BMIM BF$_4$ and left all night to allow the self-assembling of the membrane. The results were not as expected, and the membrane was not mechanically stable even after drying.
- The use of CMC as binder decreases the crack domains considerably, no longer visible in natural light but still visible by pointing a torch behind the membrane (membrane 8). In addition, membranes with CMC are much more resistant to bending (on flexible

filters as PES), and do not show any sign of damage even with complete bending (membrane 9 in **figure 4.4 d**).

- After the membrane number 16, the slurry of MoS_2 dispersed in distilled water and held into the refrigerator run out, therefore, it was used the lyophilized MoS_2. Since it was impossible to redisperse it in DI-Water, we decided to use DMSO. The lyophilized MoS_2 contains a fraction of smaller flakes when compared with the one in water suspension. In fact, when used a 0.02 μm filter a fraction of the flakes passed through.

- The DMSO solvent allowed to try PVDF as binder, the membrane had improved homogeneity, but it was not possible to separate it from the alumina (0.02 μm) filter.

- None of the filtered membranes gave any sign on separating from the filter to obtain a self-standing membrane, the next approach involved the use of GO instead of binders, by mixing it with MoS_2 or filtering a double membrane (first GO and then MoS_2). The GO is less environmentally friendly than the cellulose binders, but it has a good tendency of producing self-standing membrane.
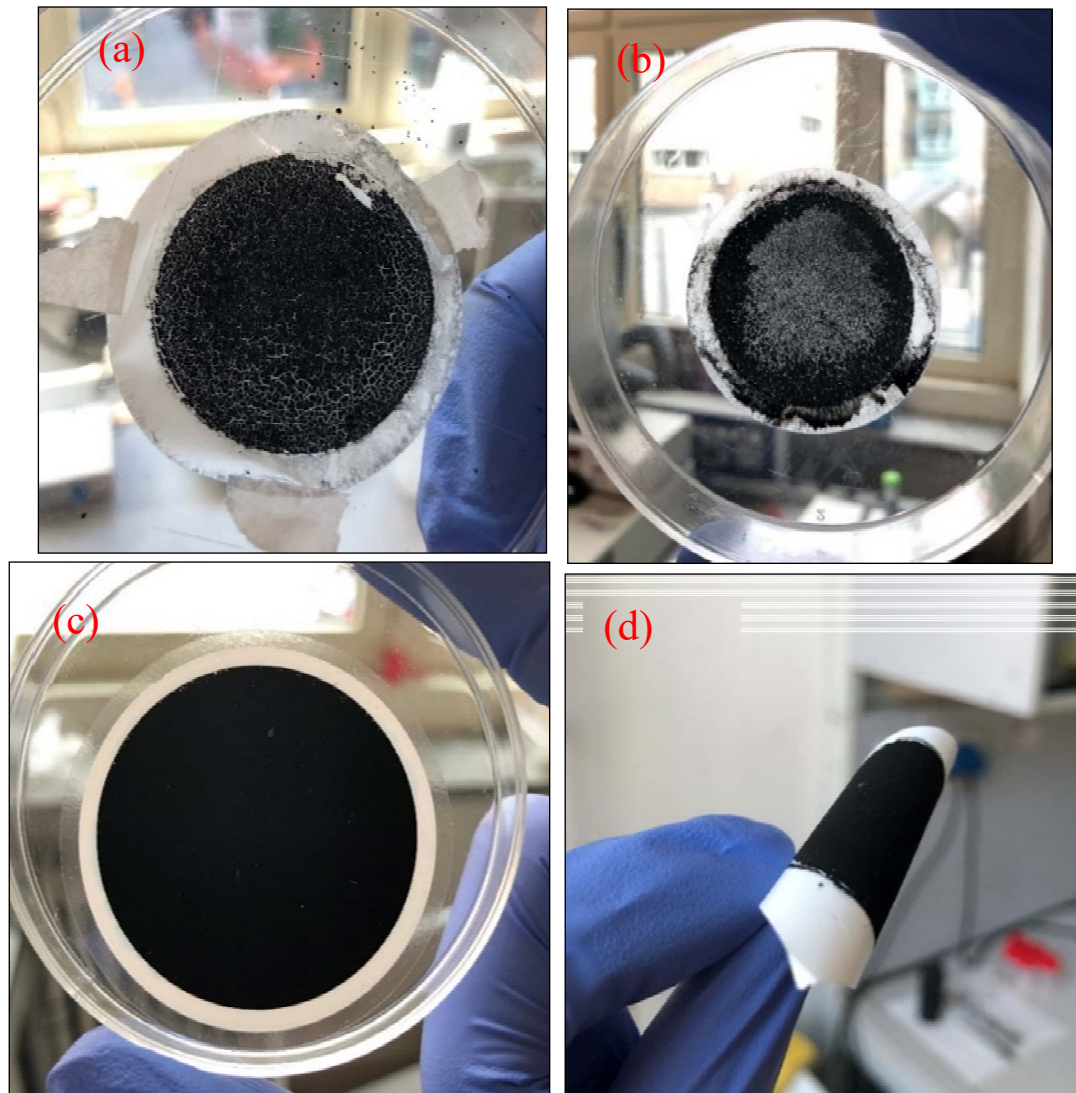

Figure 4.4: Membranes 3 (a), 7 (b), 8 (c) and 9 (d).

The first self-standing membrane produced is the number 19 (**figure 4.5 b**), with 20mg of MoS_2 and 10mg GO (2:1). During the drying process, the membrane contracts. Wrinkling has not been observed in membranes produced with the GO alone, therefore the addition of the MoS_2 was determinant. If not enough GO is used, the contraction of the MoS_2 can cause the membrane to break. The lack of GO doesn't allow the membrane to peel off from the filter. As reference for the analysis, it was produced also a membrane only with GO (number 22).

Despite the successful self-standing membrane, the characterization was problematic because of the low mechanical stability. The production of new membranes with more GO, 20mg MoS_2 and 15mg GO (number 28) was a first attempt to improve the mechanical properties of the membrane, but the filtration was too long. A mechanically stable membrane was then filtered with 15mg MoS_2 and 10mg GO (number 29) with a percentage of 60% MoS_2 (**figure 4.5 d**).
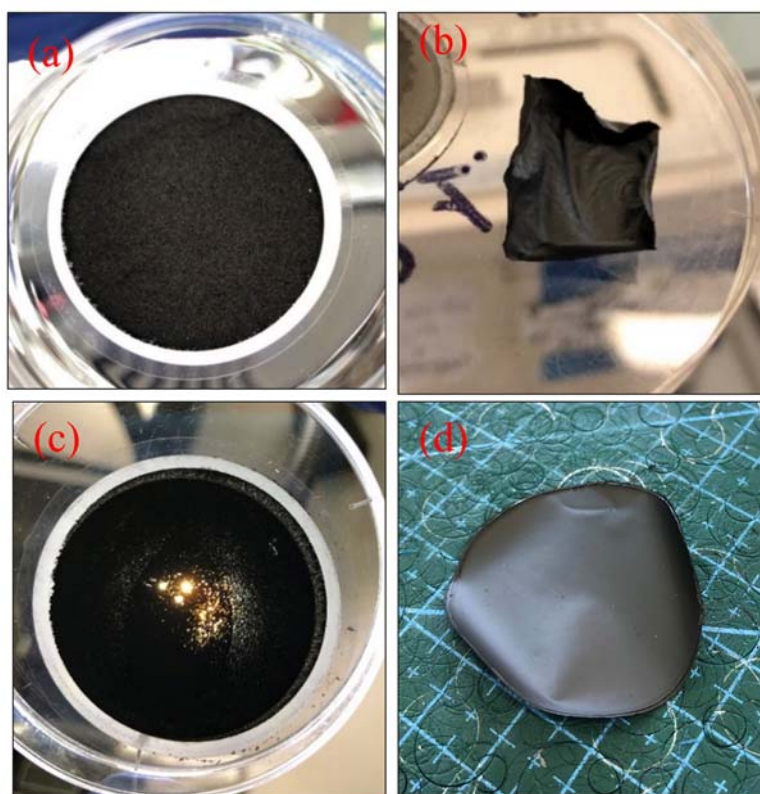

Figure 4.5: Membrane 1 (a) and 19 (b), 17 (c) and membrane 29 (1.5:1 MoS_2/GO) (d).

4.3 Physical Characterization

4.3.1 FESEM (Field Emission Scanning Electron Microscopy)

From the cross-sectional view (**figure 4.7**) of the membrane number 19 with the in-lens secondary electron detector, it is possible to distinguish the GO as the brighter lamellae structures and in between the MoS$_2$ flakes, these images show that the MoS$_2$ wasn't structured as parallel flakes and this morphology is coherent with the difficulties in filtering membranes of MoS$_2$ alone, since it doesn't stack like GO does.

Figure 4.7 in the bigger magnification shows the morphology of the MoS$_2$ clusters, the flakes are observable, but they are incorporated in a sphere-like structure that doesn't allow them to stack one parallel to each other. Many other studies on 1T-MoS$_2$ find a similar structure to this [99] and usually implies a hybrid composition phase 1T-2H MoS$_2$ only partially exfoliated, while only a few managed to produce completely exfoliated flakes [78].

The EDS map from the top view in **figure 4.6** shows a good homogeneity of the materials and the images of the dry lyophilized powder of MoS$_2$ result coherent with the material after filtration (**figure 4.9**) because it can be observed the same structure observed in the membrane.

The average thickness of the membrane is 19μm and the average size of the flakes aggregates is 260nm.
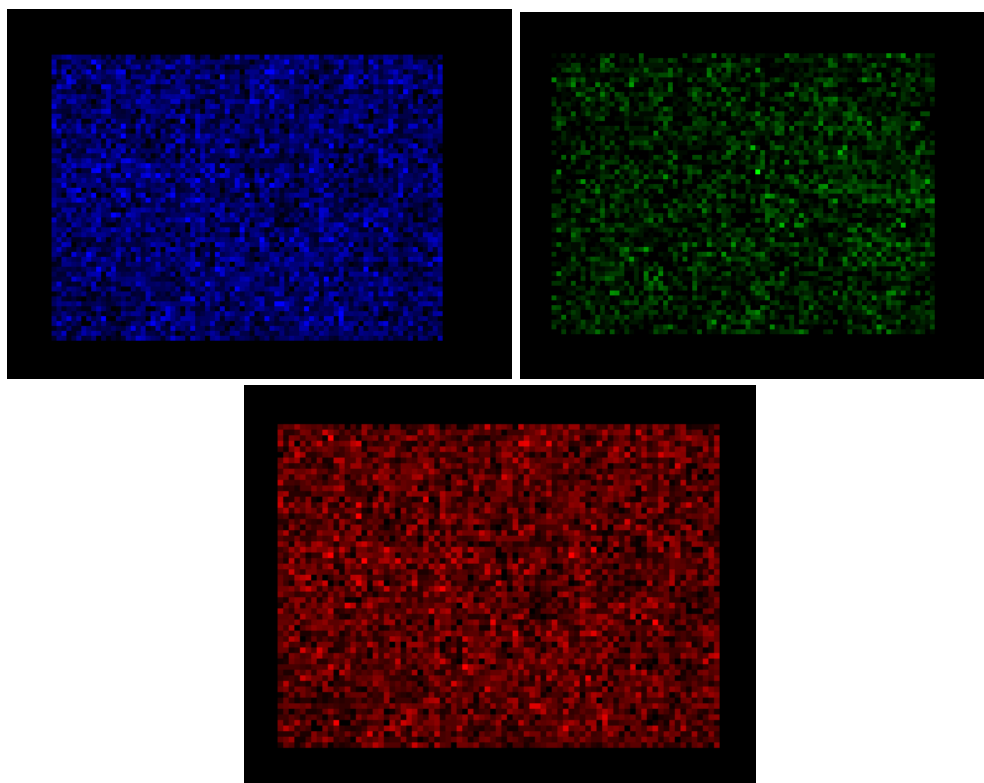

Figure 4.6: Element mapping of MoS$_2$/GO membrane view from above (Green: C, Red: Mo, Blue: S)
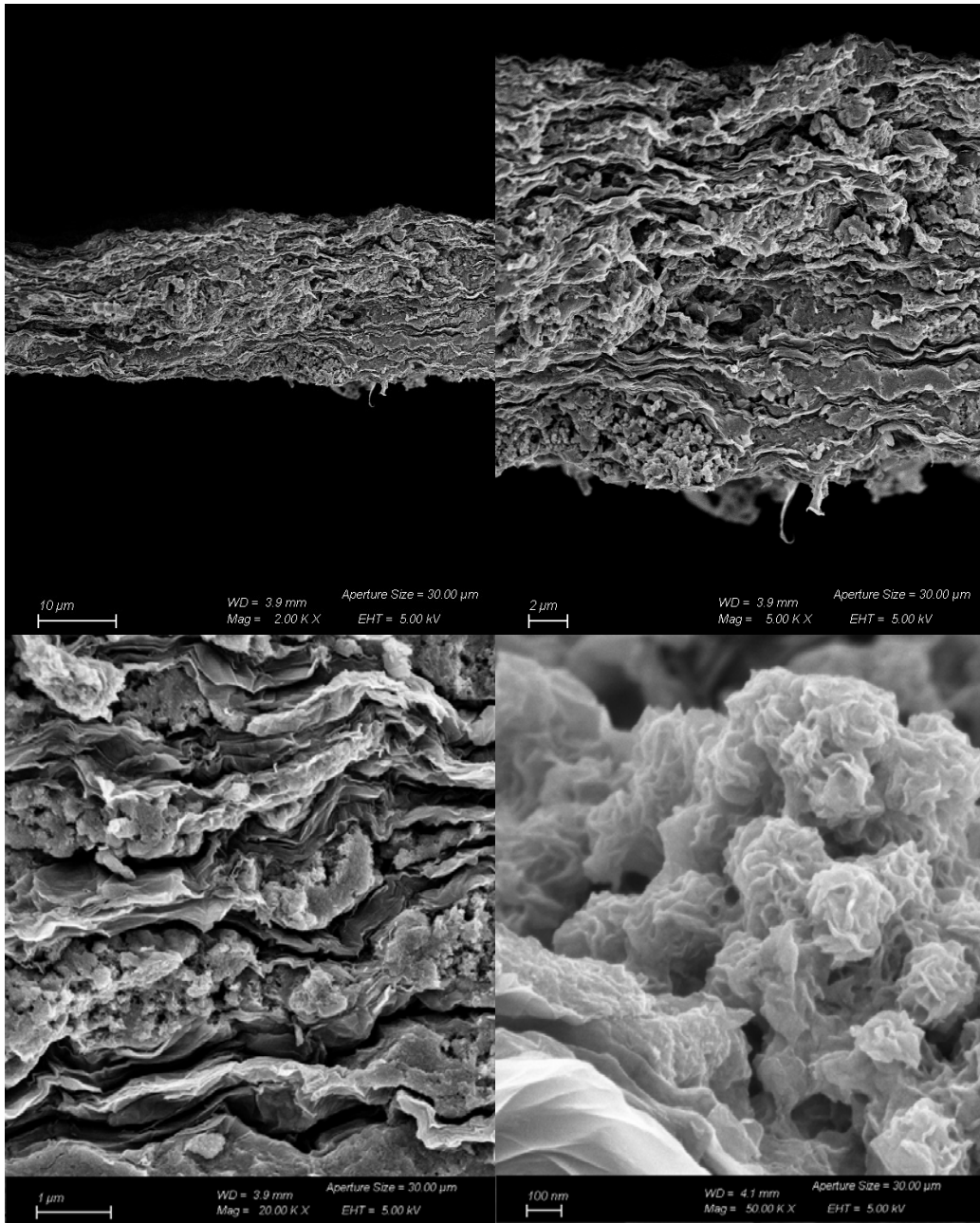
Figure 4.7: FESEM images of the cross-sectional view of the MoS₂/GO membranes at different magnitudes from 2˙000x to 50˙000x.
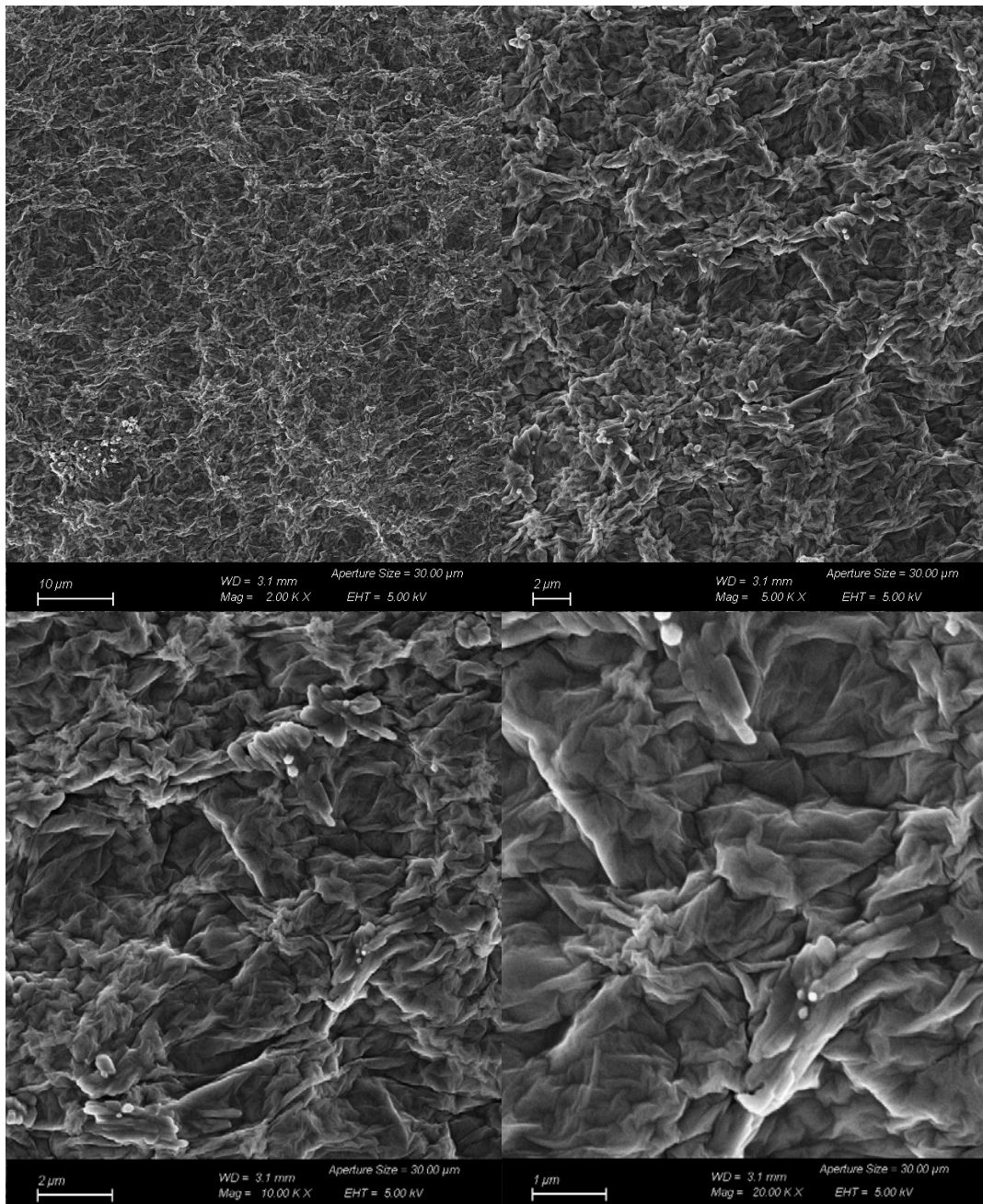
Figure 4.8: FESEM image of the MoS$_2$/GO membrane top view at different magnitudes from 2˙000x to 20˙000x.
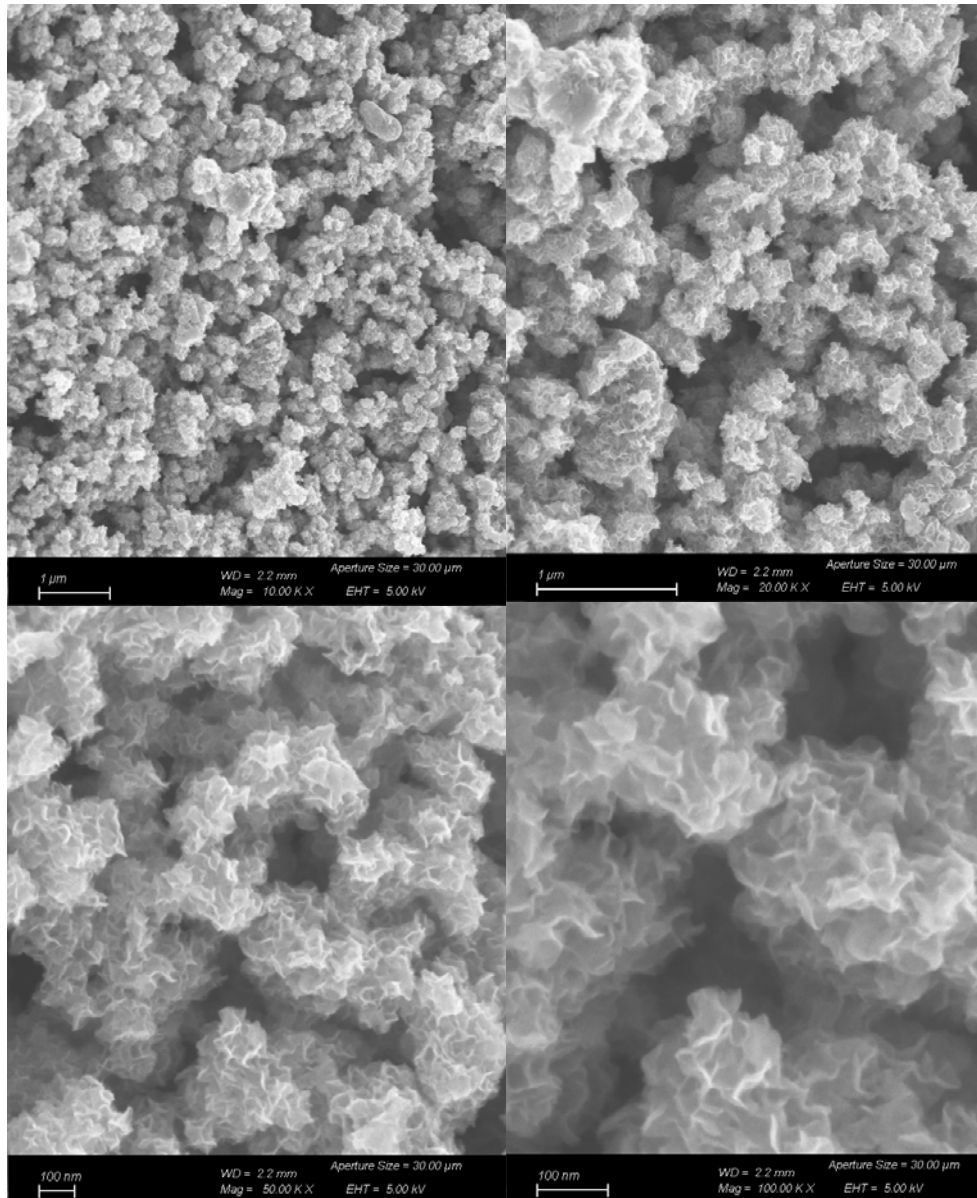
Figure 4.9: FESEM images of the MoS$_2$ lyophilized powder with different magnitudes from 10'000x (left) to 100'000x (right).

4.3.2 XRD (X-ray Diffraction)

The GO specific peak is typically around 10 degrees [101] while the MoS$_2$ peak to take in consideration is the one relative to the (002) plane, depends on the phases and it's around 9 degrees for 1T-MoS$_2$ and 14 degrees for 2H-MoS$_2$ [82].

The spacing is calculated using the Bragg law (8), considering that wet membranes have larger spacing than dried ones.

GO peak corresponding to the (001) orientation is observable at 8.67° in **figure 4.10**, the peak corresponds to a spacing of 1.019nm. The MoS$_2$/GO membrane has an additional peak

corresponding to the plane (002) of the MoS$_2$ at 6.11° which corresponds to a spacing of 1.448nm (**figure 4.10**), this spacing suggests the presence 1T-MoS$_2$ exfoliated phase, but this distance is larger than expected from a dry MoS$_2$ membrane which should be around 1nm or lower (depends on the intercalation of ions and content of solvent still adsorbed) [82]. The larger spacing can be attributed to water molecules still adsorbed, or the DMSO (used as solvent for the filtration that didn't get removed in the BUCHI oven at 80°C) [102]. The broad peaks of the MoS$_2$ confirm the nanosized dimension of the domains which is in agreement with morphology in which the flaxes are few nanometres large.

In the MoS$_2$ sample, the peak relative to the (002) orientation is found at 10.27° degrees, this represents an interlayer spacing of 0.432nm which is in agreement with other reported values [103,104]. As the MoS$_2$/GO membranes, the peaks broadening suggests a short range order due to the nanosized structures.
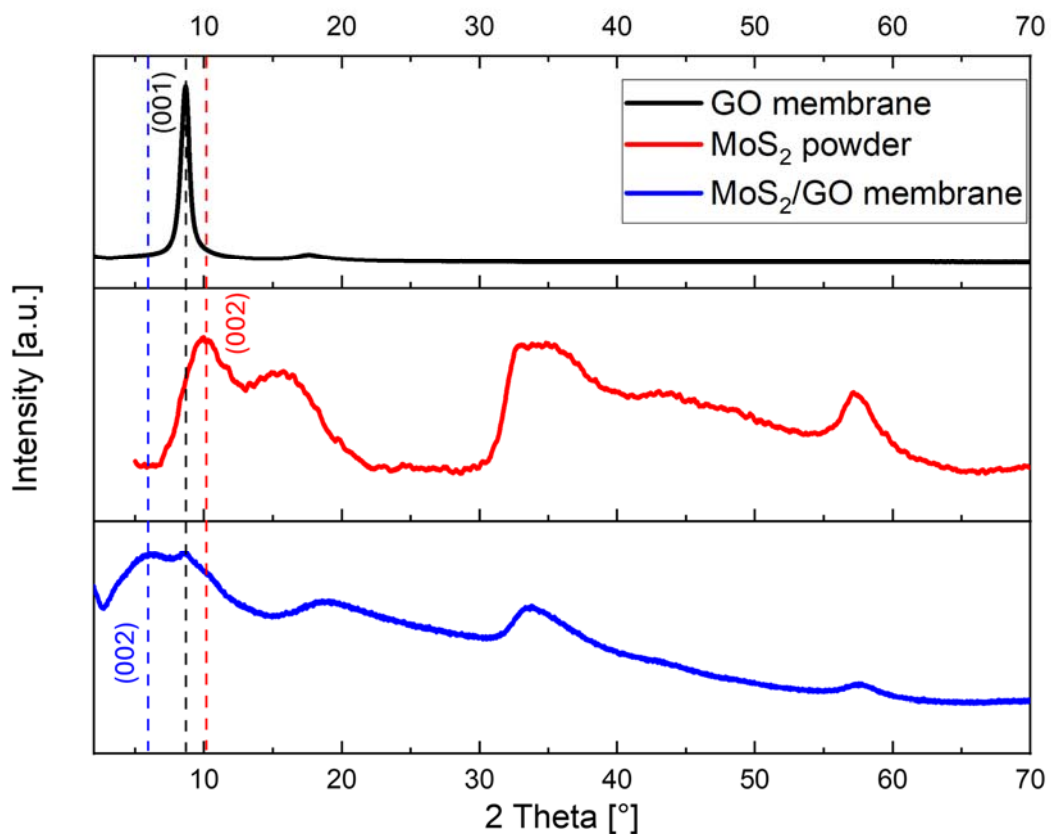

Figure 4.10: XRD patterns of the MoS$_2$/GO membrane (MoS$_2$ —). XRD patterns of the GO membrane (GO —). XRD patterns of the MoS$_2$-Na lyophilized powder (MoS$_2$ —).

4.4 Ionic Resistance

Following the method and setup in chapter 3.4.4, ionic resistance measurements were performed with two different salts, KCl and NaCl both 0.5M in concentrations. The measurements are showed in the **table 4.3, 4.4** expressed only in Ohm. The measures are EIS, linear sweep voltammetry galvanostatic and linear sweep voltammetry potentiostatic, **figure 4.12,13,14** show and example of the 3 graphs where the data are obtained.

In **figure 4.11** there are represented the values of the membrane's resistances calculate with the equation (13). It is necessary to consider that the thickness plays an important role being directly proportional to the resistance.

The resistance towards K^+ seems to be higher than of Na^+, while it has been observed the opposite in another work [105]. A good IEM is expected to have high permselectivity and low ionic resistance, the value for the MoS_2/GO membrane could be considered good if compared to the values for GO membranes of other works [94], but this value is valid only if also the permselectivity is high.

Table 4.3: Ionic resistance measured for KCl 0.5M: EIS, linear sweep voltammetry galvanostatic, linear sweep voltammetry potentiostatic and the average of the three.

	Ω			
	EIS	Pot	Galv	Avg
No membrane	3.140	3.220	3.247	3.202
GO	5.754	5.848	5.753	5.785
MoS_2/GO	5.950	5.745	5.649	5.781

Table 4.4: Ionic resistance measured for NaCl 0.5M: EIS, linear sweep voltammetry galvanostatic, linear sweep voltammetry potentiostatic and the average of the three.

	Ω			
	EIS	Pot	Galv	Avg
No membrane	4.127	4.177	4.172	4.159
GO	5.908	6.023	5.903	5.945
MoS_2/GO	4.485	5.029	4.993	4.836
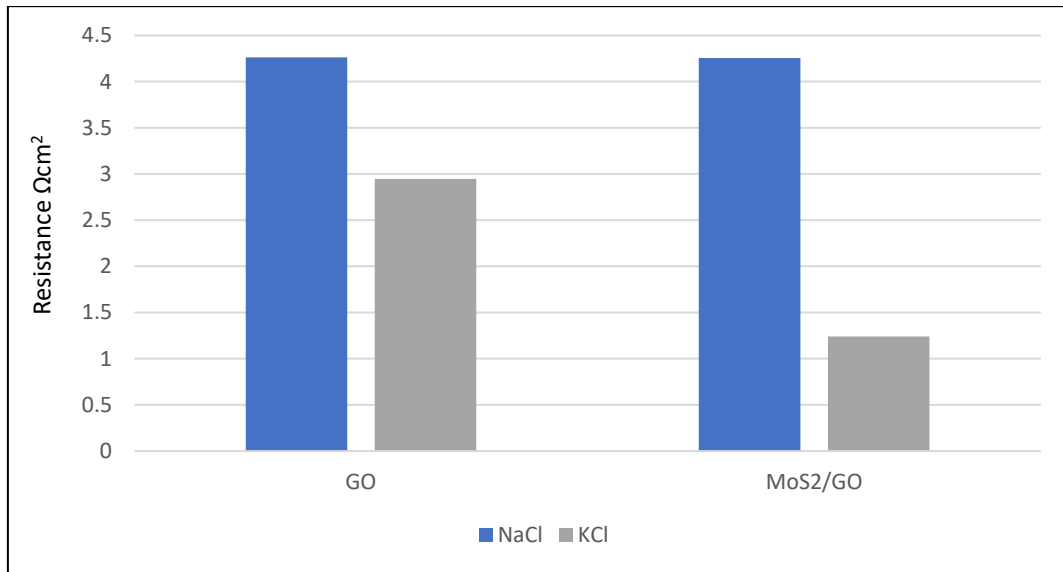
Figure 4.11: Average areal ionic resistance of the GO and MoS$_2$/GO membranes in the different electrolytes.
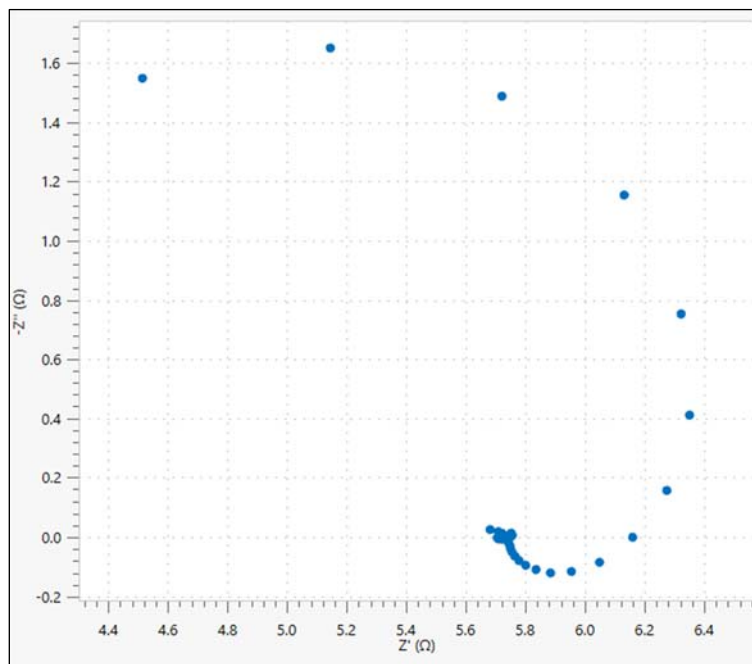
Figure 4.12: Example of IES for GO membrane with KCl 0.5M
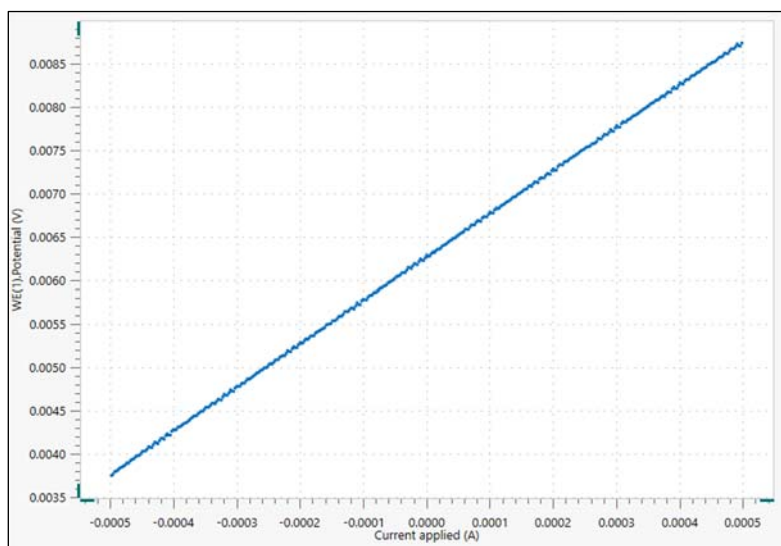
Figure 4.13: Example of linear sweep voltammetry galvanostatic for MoS$_2$/GO membrane with NaCl 0.5M.
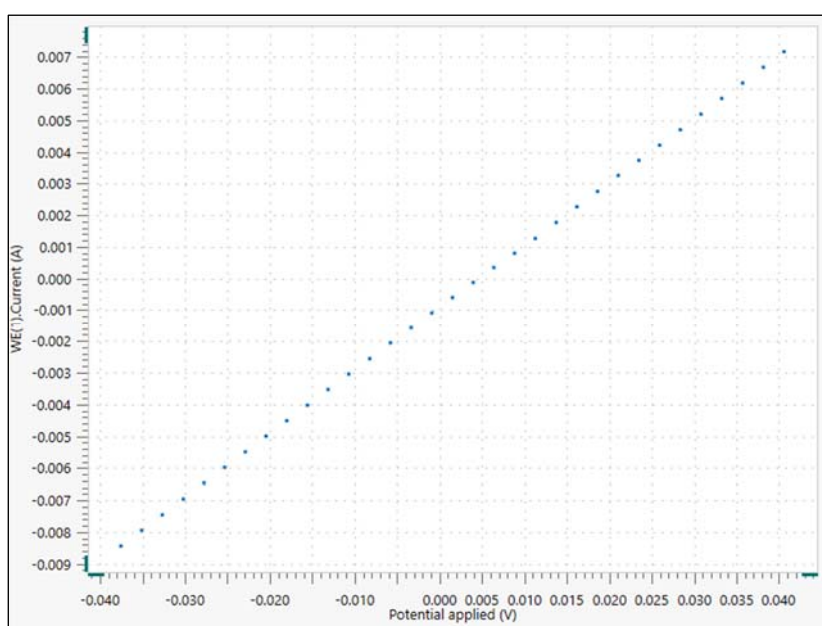
Figure 4.14: Example of linear sweep voltammetry potentiostatic for MoS$_2$/GO membrane with NaCl 0.5M.

4.5 Permselectivity

The measurements for the permselectivities were performed in the setup previousy illustrated in chapter 3.4.3. The **figure 4.15** shows the permselectivieties of the GO and MoS$_2$/GO membranes in the different electrolytes while the **table 4.5, 4.6** and **4.7** contain the measurements and the apparent permesectivities. The MoS$_2$/GO membrane compared to GO

exhibits similar permselectivity with KCl, higher with NaCl and lower with LiCl. The porosity due to the poor stacking of the MoS_2 could be the main reason of the poor permselectivity of the MoS_2/GO membranes, these membranes tend to pierce quite early during the measurement, which made the collection of data difficult, only one membrane with higher values, used to measure the permselectivity for KCl didn't pierce at all, conserving its mechanical stability even after the measurement making possible to remove it from the set up still intact.
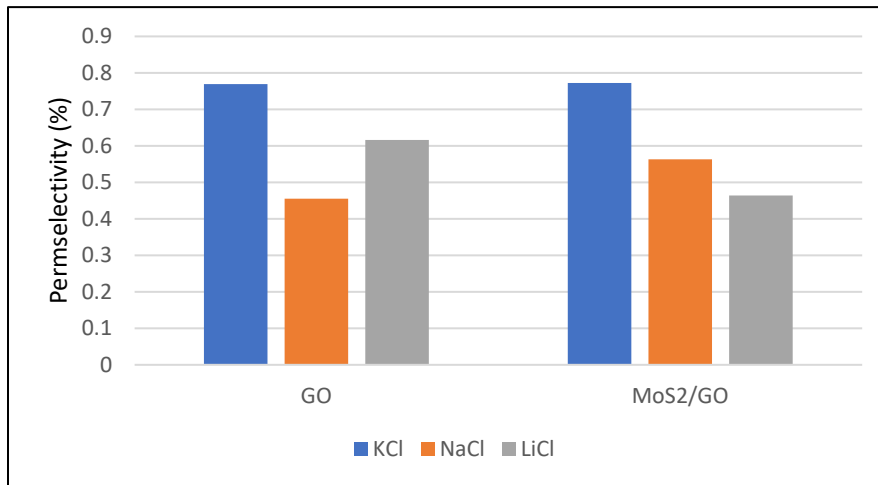
Figure 4.15: Apparent permselectivities of GO and MoS_2/GO membranes with the ion transport numbers taken into account for three different electrolytes (KCl blue, NaCl orange, LiCl grey).

Table 4.5: Potentials of the membranes with KCl

	E_{offset} (mV)	E_{meas} (mV)	E_{mem} (mV)	α_{ap} (%)	α_{tn} (%)
GO	6	33.5 mV	28.3	76.5	76.9
MoS_2/GO	6	34.4 mV	28.4	76.78	77.2

Table 4.6: Potentials of the membranes with NaCl

	E_{offset} (mV)	E_{meas} (mV)	E_{mem} (mV)	α_{ap} (%)	α_{tn} (%)
GO	6	18.92	12.92	34.12	45.46
MoS_2/GO	6	22.06	17.91	47.18	56.27

Table 4.7: Potentials of the membranes with LiCl

	E_{offset} (mV)	E_{meas} (mV)	E_{mem} (mV)	α_{ap} (%)	α_{tn} (%)
GO	6.5	23.50	19.43	49.02	61.61
MoS_2/GO	6.5	15.52	11.45	28.88	46.45

The transport of ions may not be as expected on 2D lamellar membranes according to Lu et al. [106], the mass transport within nanochannels of lamellar 2D films does not really occur as intended but rather, it is the microporous defects that are the results of imperfect stacking due to poor fabrication process that dominate the mass transport. In this case, the porosity due to the poor stacking of the MoS2 could be a reason for the lower permselectivity of the MoS2/GO membranes. The thickness of the membrane plays an important role in the permselectivity, thinner membranes are less permselective than thicker ones [94].

Both GO and MoS2/GO membranes show a lower Li^+ ions permselectivity with respect to Na^+ ions, the size of the alkali metals are $Li^+ < Na^+ < K^+$ but their hydration shell follows the opposite scale $Li^+ > Na^+ > K^+$, this may contribute on a steric hindrance.

The results are not sufficient for a good permselective membrane (usually above 95%) but thanks to a more appropriate morphology of the MoS2 flakes, better stacking could be achieved improving drastically the permselectivity of the membranes.

4.6 Energy Storage

In order to understand whether the self-standing membrane has potentialities as electrode for energy storage, the MoS2 synthetized as previously described was used either as active material (70%) in standard electrodes and as self-standing electrode of MoS2/GO (membrane 19) in coin-cell configuration with the MoS2-based material at the working electrode and metallic Li as counter and reference electrode in a half-cell.

The standard electrodes with MoS2 (70%) and the self-standing electrodes with MoS2/GO were cycled between 1 and 3 V vs. Li/Li+ to avoid the irreversible formation of metallic Mo and Li2S at lower potential:

$$Li_xMoS_2 + (4-x)Li^+ + (4-x)e^- \longrightarrow Mo + 2Li_2S \tag{15}$$

From the cyclic voltammetry of the MoS2 (70%) electrode in **figure 4.16-a** it is possible to observe two distinct peaks: a broad reduction peak with a maximum at 1.75V and an oxidation peak at about 2.25V corresponding to the reversible intercalation and deintercalation of Li^+ ions with the formation of Li_xMoS_2:

$$MoS_2 + x\,Li^+ + x\,e^- \underset{\leftarrow}{\overset{\rightarrow}{}} Li_xMoS_2 \tag{16}$$

From **figure 4.16-b** it is possible to observe that the peak separation is low indicating a quasi-reversible electrochemical process. For potential lower than 1.5 V, the CV looks more rectangular, suggesting that there is a large electric double layer (EDL) formation, and this is consistent with literature data [103,107].
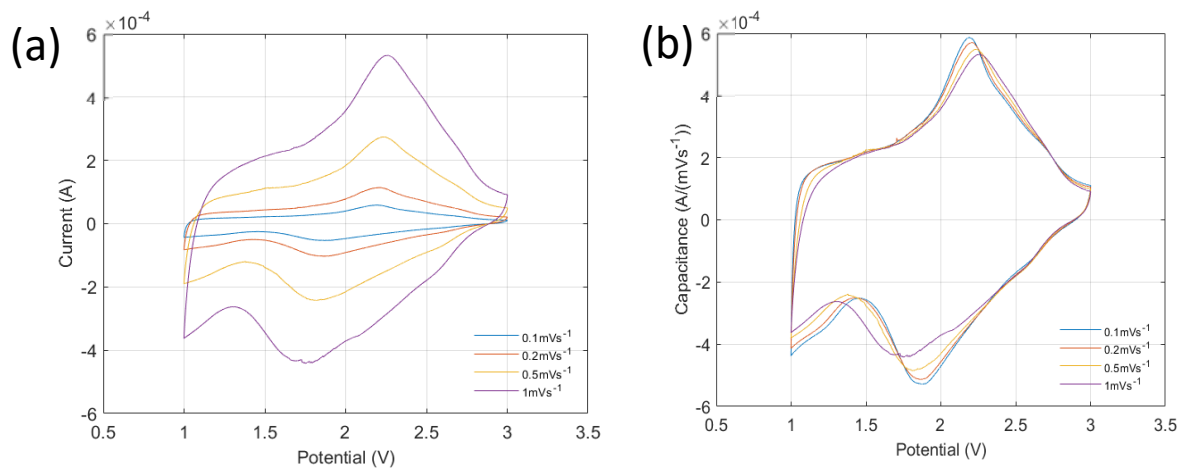
Figure 4.16.: (a) Cyclic voltammetry and (b) reconstructed for the MoS$_2$ (70%) electrode at different scan-rates.

From the same graph it was estimated the Coulombic efficiency and the rate capability from 0.1 to 1 mV/s, as shown in **figure 4.17-a,b** respectively. It is possible to observe that the efficiency was for all the rates superior to 98.6% and that capacity was almost constant with the scan rate (from 280 mAh/g at 0.1mV/s t o265 mAh/g at 1mV/s).
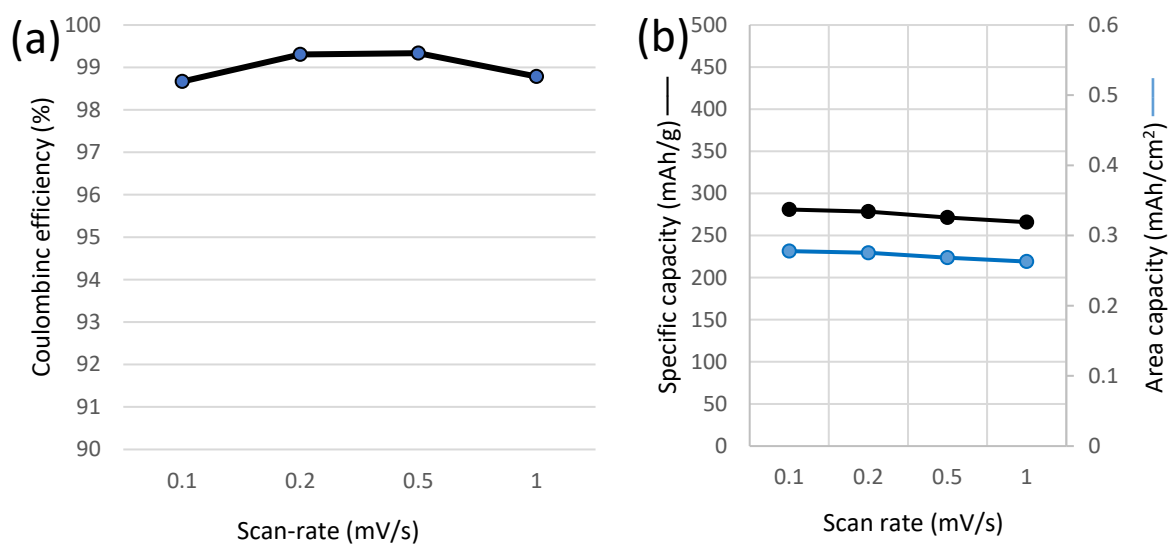
Figure 4.17: (a) coulombic efficiency for the MoS$_2$ (70%) electrode at different scan rates. (b) Specific capacity ⎯⎯ and area capacity ⎯⎯.
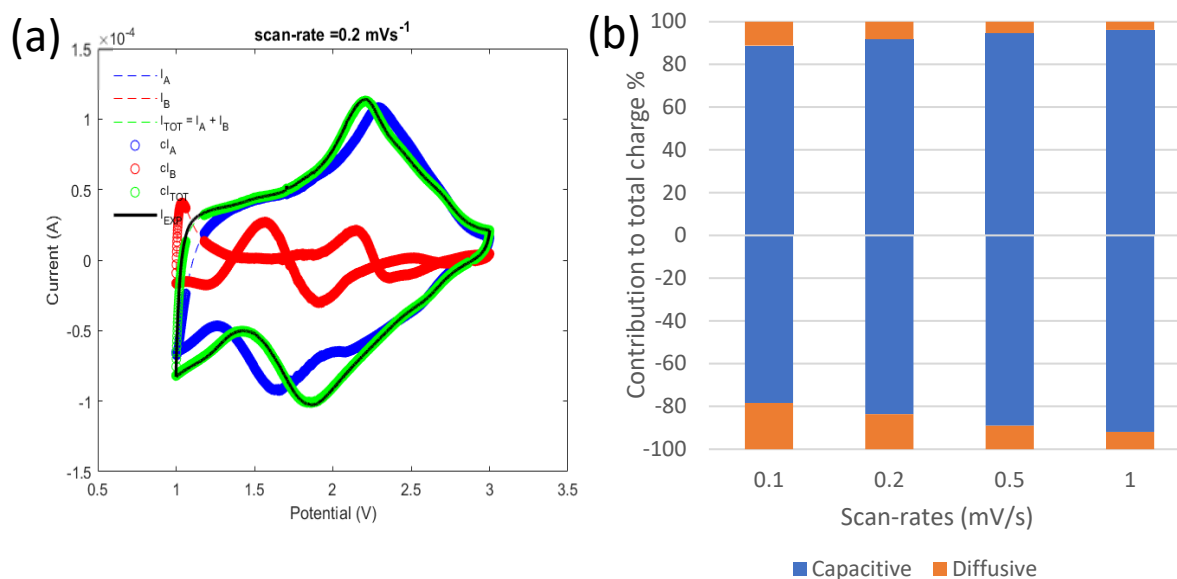
Figure 4.18: (s) voltammogram at 0.2 mV/s with the deconvolution of the capacitive behaviour (blue) and diffusive behaviour (red), in black the experimental data and the sum of the two in green. (b) Quantification of the diffusive and capacitive contribute for the cathodic current (negative) and anodic current (positive).

Therefore, according to the previously described method of Dunn in paragraph 3.4.2, the CV were analysed at different scan rates in order to visualize and quantify the capacitive and non-capacitive behaviours of the electrode. In **figure 4.18-a** the recorded voltammogam at 0.2 mV/s is represented by the black data points (I_{exp}). In blue, instead the datapoint are those of the capacitive-controlled currents (I_A) and the red of the diffusion-controlled currents (I_B) according to the equation (4) in paragraph 3.4.2. The sum of the two is the green line ($I_{TOT} = I_A + I_B$) which has to overlap the black line. From the reconstructed voltammetries it is possible to confirm that the behaviour of the MoS_2 (70%) electrode is mainly capacitive.

Identical data analysis was performed on the electrodes cut from the self-standing membrane: in the left-hand side graph of **figure 4.19-a,** it is possible to observe the raw CV at scan rates ranging from 0.1 mV/s to 1 mV/s and on the graph at the right-hand the same data are reported normalized with respect to the scan rate at which the CV were recorded. From this visualization it is possible to observe a different trend with respect to the behaviour of the pure MoS_2 electrodes. In fact, the normalized data of the self-standing electrodes do not overlap suggesting non-capacitive storage mechanisms.
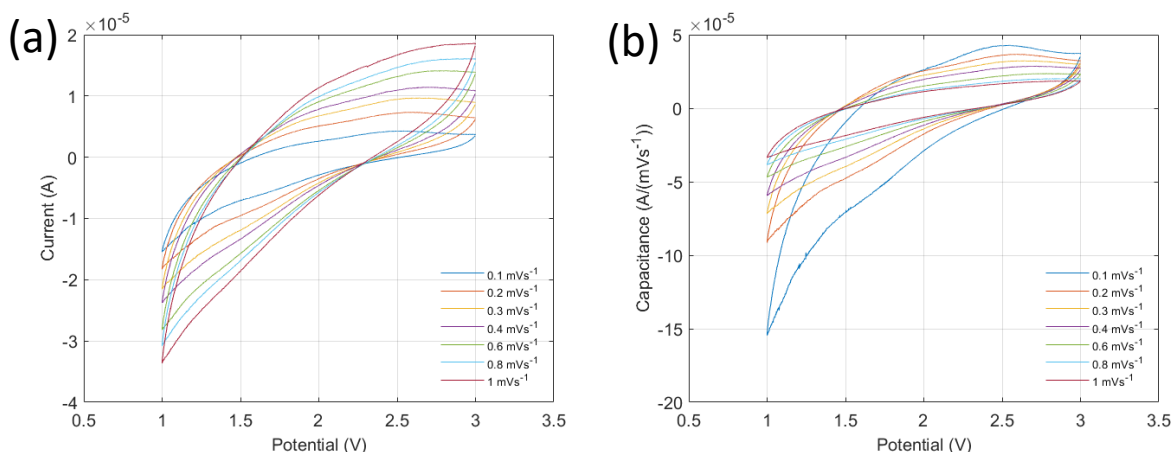
Figure 4.19: (a) Cyclic voltammetry and (b) Cyclic voltammetry and reconstructed for the MoS$_2$/GO electrodes at different scan-rates.

The CV from the MoS$_2$/GO electrode (**figure 4.19**) show a highly distorted shape indicating a resistive behaviour. Moreover, no clear redox peaks in CV are present, even if at 2.5 V in the anodic and at –1.6 V in the cathodic scan two broad peaks are visible. They show an important shift between the charging and discharging potential of the peaks, indicating also electrochemical irreversibility. The main reasons for this behaviour can be a poor contact in between the MoS$_2$ flakes which limits the percolation of the electrons and charges.
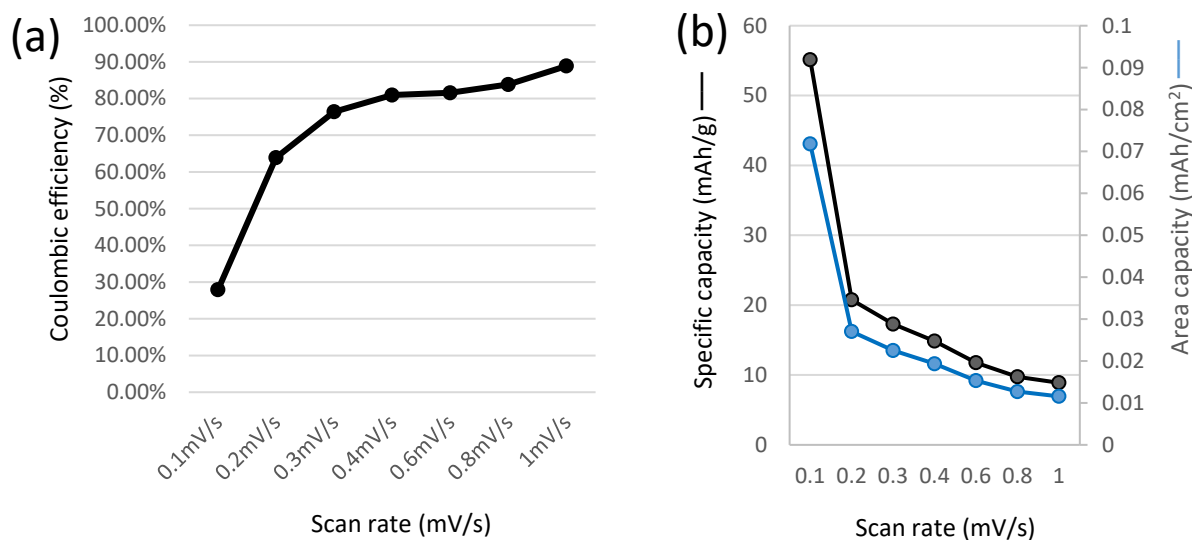
Figure 4.20: (a) coulombic efficiency for the MoS$_2$/GO electrode at different scan rates. (b) Specific capacity ⸻ and area capacity ⸻.

The Coulombic efficiency and the rate capability from 0.1 to 1 mV/s, are shown in **figure 4.20-a,b** respectively. It is possible to observe that the efficiency increases with the scan-rate, suggesting that irreversible reactions al low scan rates are predominant with respect to the

storage. Moreover, from the discharge part of the voltammograms it is possible to observe that capacity is strongly decreasing with the scan rate. Indeed, this trend can be linked to the high resistivity of the self-standing electrodes themselves.
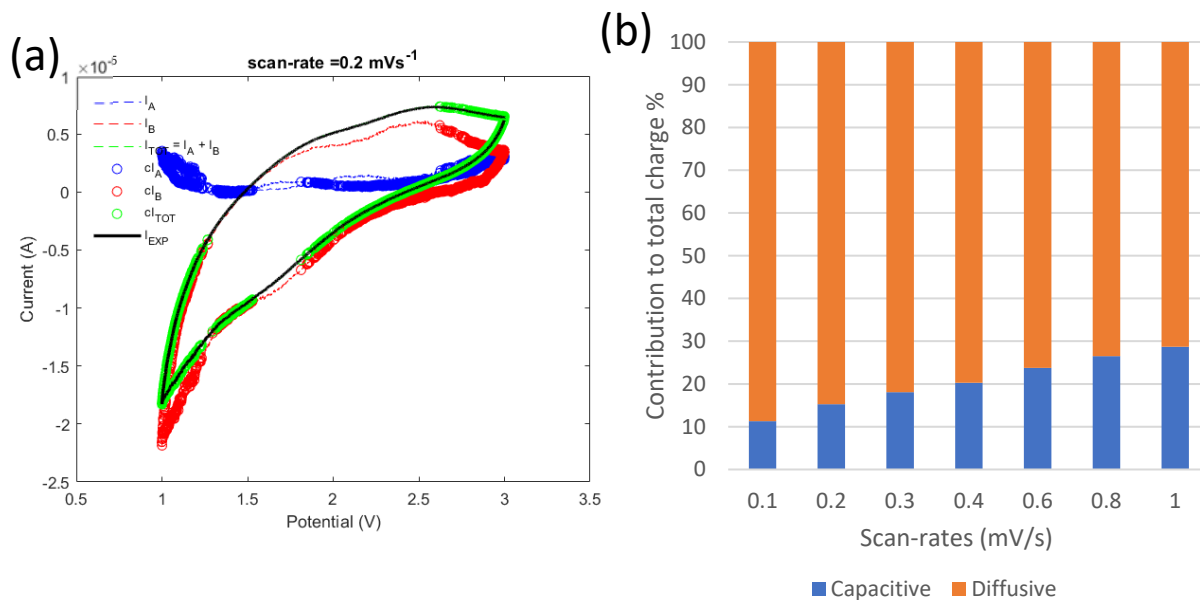

Figure 4.21: (a) kinetic analysis of the MoS$_2$/GO electrode at 0.2 mV/s scan rate: the black line is the experimental data, red is the diffusive contribute, blue is the capacitive contribute, green is the sum of blue and red. (b) Quantification of the diffusive and capacitive contribute for the cathodic current.

In order to unravel if the storage or delivered energy have a capacitive or diffusive main behaviours, the kinetic analysis was performed and reported in **figure 4.21**. From the left-hand graph in which the reconstructed voltammetries are shown together with the original data (black) it is possible to observe that only the cathodic scan satisfies the imposed trend of the Dunn's analysis while the anodic scan is not following that trend. This is visible by the missing datapoints in that part of the graphs. Still, from the reconstructed voltmmograms it is possible to observe that the storage (cathodic scan) proceeds by diffusion-controlled mechanisms while, as previously mentioned, the delivered (anodic scan) charge is not following any storage dependence, therefore suggesting that during the anodic scan the electrocatalytic processes play the major rule. In the cathodic scan, the region between 1.5 and 2 V do not follow the storage trends, suggesting that also in this potential range electrocatalytic processes dominate.

The specific capacity values for MoS$_2$ in organic electrolyte (**figure 4.20**) are similar to the values (20.81 mAh/g) from Parthiban et al. [108]. Also, if compared to GO electrode measurements with LiPF$_6$ [109], this work has lower currents by one order of magnitude, but similar specific capacity.

Another study measured the electrochemical properties of a composite electrode MoS$_2$/GO [110] but at higher scan rates (50mV/s) with 0.1M LiPF$_6$, in this case currents were one order

of magnitude lower than in these experiments. They observed cathodic peaks at 1.48V and 3.2V, and one anodic peak at 1.39V for MoS$_2$ while cathodic and anodic peaks at 1.1V 2.6V 3.2V for GO. These peaks shift when combining the two materials in different quantities suggesting poor electrochemical reversibility.

Moreover, with this type of electrodes the Dunn's method is no longer valid, also because of the high resistivity of the membrane that is not taken into account in the whole model. It is important to take into consideration that GO is not electrically conductive as 1T-MoS$_2$, and this can result in worse performance of the hybrid membrane, and the stacking of GO can even interrupt the percolation of the MoS$_2$ influencing even more the percolation of the charges.

A more accurate method to analyse such material could be the SPECS or the MUSCA, as mentioned in paragraph 3.4.2 among the other simple methods. Both, in fact, take into the account a third component that is called "residual" in which falls multiple contributions.

Reducing the GO into rGO could improve the electronic performance, but the reaction could cause the oxidation of MoS$_2$ as suggested by Wang et. al [111]:

$$GO + MoS_2 \rightarrow rGO + MoO_4^{2-} + 2SO_4^{2-} \tag{17}$$

Even though it has been proved the possibility to make a stable rGO/MoS$_2$ composite for water-based supercapacitors [112], membranes have never been produced with the same synthesis (and without binders) because they were mechanically unstable.

Muharrem A. et al. [78] Studied the 1T MoS$_2$ and concluded that the intercalation processes are slower in organic electrolytes, since 1T MoS$_2$ is hydrophillic and the organic electrolytes are more hydrophobic, the intercalation process results diffusion limited as in the CV results of this work. On contrary, in Cook et al. [103,107] works, the nanosized MoS$_2$ showed an almost completely capacitive behaviour with organic electrolyte (1M LiPF$_6$ in a 1:1 EC:DMC solvent with 5% (v/v) fluorinated ethylene carbonate).

CONCLUSIONS

The literature shows a wide range of results for MoS_2 membranes and electrodes, therefore our difficulties in the production of self-standing membranes seems to be linked to the completely exfoliated $1T$-MoS_2. The 1T phase is thermodynamically unstable and only stable in coexistence with the 2H phase [113,114], this causes the production of MoS_2 only partially 1T-metallic which translate in reduced electrical performance of electrodes.

The synthesis of $1T$-MoS_2 is quite slow (12h), increasing the volumes of production was complicated because of the lack of bigger reactors, the yield of reaction was only 60%, and also due to the failed attempts to speed the synthesis by using a microwave-assisted method the only choice was to keep working with the classic hydrothermal in muffle.

The production of a self-standing was accomplished after many of tries using GO together with the MoS_2. The other membranes (non-self-standing) attempted with binders couldn't be tested supported on the filter because of the cracking in the active material.

The permselectivity and ionic resistance results are similar to the GO membrane but considering of the bad stacking of the MoS_2/GO there is a big margin of improvement for the studied membrane. Higher values of permselectivity were measured with Na^+ ions, but the main reason seems to be a membrane with higher mechanical performance More ions, even bivalent ions, could be tested for permselectivity in perspective to the recovery of valuable metals.

Energy storage measurements show that the MoS_2 itself behaves as a pure pseudocapacitor, showing very little diffusive-controlled charge accumulation even at 0.1 mV/s. The self-standing electrodes of MoS_2/GO instead, show diffusive behaviour and high electrical resistivity with minor capacitive accumulation of charges. The data showed low coulombic efficiency at low scan rates, suggesting the presence of irreversible reaction at the MoS_2/GO electrode.

A potential solution to the scalability of the synthesis could be found in the microwave-assisted synthesis by using a different solvent or by trying to change one of the reagents. A successful microwave-assisted synthesis would increase substantially the production of material and possibly even the yield of the reaction while maintaining the process still on a laboratory scale.

Further investigations towards the synthesis of a completely exfoliated MoS_2, with larger flakes dimensions or with functionalization could help with the production of a self-standing membrane without the help of GO or any binder at all, allowing to exploit at full the good performance of the of the material as the we observed on the MoS_2 (70%) electrodes.

BIBLIOGRAPHY

[1]   Perreault, François, et al. "Environmental Applications of Graphene-Based Nanomaterials." Chemical Society Reviews, vol. 44, no. 16, 2015, pp. 5861–96, https://doi.org/10.1039/c5cs00021a.

[2]   Asadollahi, Mahdieh, et al. "Enhancement of Surface Properties and Performance of Reverse Osmosis Membranes after Surface Modification: A Review." Desalination, vol. 420, 2017, pp. 330–83, https://doi.org/10.1016/j.desal.2017.05.027.

[3]   Faculty TA, Qiu S, Fulfillment IP. Synthesis and characterization of phase inversion membrane with Mos2 Copyright © 2019 By Sihan Qiu synthesis and characterization of phase inversion 2019.

[4]   Loske, Lara, et al. "2D Nanocomposite Membranes: Water Purification and Fouling Mitigation." *Membranes (Basel)*, vol. 10, no. 10, 2020, pp. 295-, https://doi.org/10.3390/membranes10100295.

[5]   Liu, Yang, et al. "MoS2-Based Membranes in Water Treatment and Purification." Chemical Engineering Journal (Lausanne, Switzerland : 1996), vol. 422, 2021, pp. 130082-, https://doi.org/10.1016/j.cej.2021.130082.

[6]   Hailemariam, Ruth Habte, et al. "Reverse Osmosis Membrane Fabrication and Modification Technologies and Future Trends: A Review." *Advances in Colloid and Interface Science*, vol. 276, 2020, pp. 102100–102100, https://doi.org/10.1016/j.cis.2019.102100.

[7]   Peñate, Baltasar, and Lourdes García-Rodríguez. "Current Trends and Future Prospects in the Design of Seawater Reverse Osmosis Desalination Technology." *Desalination*, vol. 284, no. 4, 2012, pp. 1–8, https://doi.org/10.1016/j.desal.2011.09.010.

[8]   https://commission.europa.eu/strategy-and-policy/priorities-2019-2024/european-green-deal/energy-and-green-deal_en

[9]   Iqbal, Muhammad Zahir, and Umer Aziz. "Supercapattery: Merging of Battery-Supercapacitor Electrodes for Hybrid Energy Storage Devices." *Journal of Energy Storage*, vol. 46, 2022, pp. 103823-, https://doi.org/10.1016/j.est.2021.103823.

[10]   Anh Tran, Vy, et al. "Metal-Organic Framework for Lithium and Sodium-Ion Batteries: Progress and Perspectivez." *Fuel (Guildford)*, vol. 319, 2022, pp. 123856-, https://doi.org/10.1016/j.fuel.2022.123856.

[11]   Forouzandeh, Parnia, and Suresh C. Pillai. "Two-Dimensional (2D) Electrode Materials for Supercapacitors." *Materials Today : Proceedings*, vol. 41, Elsevier Ltd, 2021, pp. 498–505, https://doi.org/10.1016/j.matpr.2020.05.233.

[12]   He, Zuoli, and Wenxiu Que. "Molybdenum Disulfide Nanomaterials: Structures, Properties, Synthesis and Recent Progress on Hydrogen Evolution Reaction." Applied Materials Today, vol. 3, 2016, pp. 23–56, https://doi.org/10.1016/j.apmt.2016.02.001.

[13]   Verweij, Hendrik. "Inorganic Membranes." *Current Opinion in Chemical Engineering*, vol. 1, no. 2, 2012, pp. 156–62, https://doi.org/10.1016/j.coche.2012.03.006.

[14] Bhave, R., 2012. *Inorganic membranes synthesis, characteristics and applications: synthesis, characteristics, and applications*. Springer Science & Business Media.

[15] Roa, F., Way, J.D., McCormick, R.L. and Paglieri, S.N., 2003. Preparation and characterization of Pd–Cu composite membranes for hydrogen separation. *Chemical Engineering Journal*, *93*(1), pp.11-22.

[16] Okazaki, J., Ikeda, T., Tanaka, D.A.P., Sato, K., Suzuki, T.M. and Mizukami, F., 2011. An investigation of thermal stability of thin palladium–silver alloy membranes for high temperature hydrogen separation. *Journal of Membrane Science*, *366*(1-2), pp.212-219.

[17] Hatlevik, Ø., Gade, S.K., Keeling, M.K., Thoen, P.M., Davidson, A.P. and Way, J.D., 2010. Palladium and palladium alloy membranes for hydrogen separation and production: History, fabrication strategies, and current performance. *Separation and Purification Technology*, *73*(1), pp.59-64.

[18] Chung, T.S., Jiang, L.Y., Li, Y. and Kulprathipanja, S., 2007. Mixed matrix membranes (MMMs) comprising organic polymers with dispersed inorganic fillers for gas separation. *Progress in polymer science*, *32*(4), pp.483-507.

[19] Aroon, M.A., Ismail, A.F., Matsuura, T. and Montazer-Rahmati, M.M., 2010. Performance studies of mixed matrix membranes for gas separation: A review. *Separation and purification Technology*, *75*(3), pp.229-242.

[20] https://www.sciencedirect.com/bookseries/membrane-science-and-technology/vol/13/suppl/C

[21] André Ayral, Anne Julbe, Vincent Rouessac, Stéphanie Roualdes, Jean Durand, Microporous Silica Membrane: Basic Principles and Recent Advances, Membrane Science and Technology, Elsevier, Volume 13, 2008, Pages 33-79, ISSN 0927-5193, ISBN 9780444530707, https://doi.org/10.1016/S0927-5193(07)13002-3.

[22] Ge, Rui, et al. "GO-Based Membranes for Desalination." *Membranes (Basel)*, vol. 13, no. 2, 2023, pp. 220-, https://doi.org/10.3390/membranes13020220.

[23] Qian, Qihui, et al. "MOF-Based Membranes for Gas Separations." *Chemical Reviews*, vol. 120, no. 16, 2020, pp. 8161–266, https://doi.org/10.1021/acs.chemrev.0c00119.

[24] Cheng, Youdong, et al. "Advances in Metal-Organic Framework-Based Membranes." *Chemical Society Reviews*, vol. 51, no. 19, 2022, pp. 83–835, https://doi.org/10.1039/d2cs00031h.

[25] Su, Yuyu, et al. "Transition Metal Dichalcogenide (TMD) Membranes with Ultrasmall Nanosheets for Ultrafast Molecule Separation." *ACS Applied Materials & Interfaces*, vol. 12, no. 40, 2020, pp. 45453–59, https://doi.org/10.1021/acsami.0c10653.

[26] Luque, Susana. (2008). *[Membrane Science and Technology] Inorganic Membranes: Synthesis, Characterization and Applications Volume 13; Industrial Applications of Porous Ceramic Membranes (Pressure-Driven Processes). 177–216.* doi:10.1016/S0927-5193(07)13006-0

[27] Khoi, Tran Minh, et al. "Selective and Continuous Ion Recovery Using Flow Electrode Capacitive Deionization with Polymer Multilayers Functionalized Ion Exchange Membrane." *Desalination*, vol. 558, 2023, pp. 116626-, https://doi.org/10.1016/j.desal.2023.116626.

[28] Casado Coterillo, Clara. (2008). *[Membrane Science and Technology] Inorganic Membranes: Synthesis, Characterization and Applications Volume 13 || Pervaporation and Gas Separation Using Microporous Membranes. 217–253.* doi:10.1016/s0927-5193(07)13007-2

[29] Yaroslavtsev, A., Stenina, I. and Golubenko, D. (2020) Membrane materials for energy production and storage. Pure and Applied Chemistry, Vol. 92 (Issue 7), pp. 1147-1157. https://doi.org/10.1515/pac-2019-1208

[30] Wei, Xiaojin, et al. "Improved Dyes Separation Performance of Reduced Graphene by Incorporation MoS_2 Nanosheets." *Journal of Industrial and Engineering Chemistry (Seoul, Korea)*, vol. 111, 2022, pp. 437–46, https://doi.org/10.1016/j.jiec.2022.04.024.

[31] Yoon HW, Cho YH, Park HB. 2016 Graphene-based membranes: status and prospects. Phil. Trans. R. Soc. A 374: 20150024. http://dx.doi.org/10.1098/rsta.2015.0024.

[32] Castelletto, Stefania, and Alberto Boretti. "Advantages, Limitations, and Future Suggestions in Studying Graphene-Based Desalination Membranes." RSC Advances, vol. 11, no. 14, 2021, pp. 7981–82, https://doi.org/10.1039/d1ra00278c.

[33] Shi, Ningqiang, et al. "Synthesis of Two-Dimensional Hexagonal Boron Nitride and Mid-Infrared Nanophotonics." *ACS Applied Electronic Materials*, vol. 5, no. 1, 2023, pp. 34–65, https://doi.org/10.1021/acsaelm.2c01083.

[34] Ma, Dangchen, et al. "Thin-Film Nanocomposite (TFN) Membranes Incorporated with Super-Hydrophilic Metal–Organic Framework (MOF) UiO-66: Toward Enhancement of Water Flux and Salt Rejection." *ACS Applied Materials & Interfaces*, vol. 9, no. 8, 2017, pp. 7523–34, https://doi.org/10.1021/acsami.6b14223.

[35] Li Y, Wu Q, Guo X, Zhang M, Chen B, Wei G, et al. Laminated selfstanding covalent organic framework membrane with uniformly distributed subnanopores for ionic and molecular sieving. Nat Commun. 2020;11:599. doi: 10.1038/s41467-019-14056-7.

[36] Li MP, Zhang X, Zhang H, Liu WL, Huang ZH, Xie F, et al. Hydrophilic yolk-shell ZIF-8 modified polyamide thin-film nanocomposite membrane with improved permeability and selectivity. Sep Purif Technol. 2020;247:116990. doi: 10.1016/j.seppur.2020.116990.

[37] Lim YJ, Goh K, Kurihara M, Wang R. Seawater desalination by reverse osmosis: Current development and future challenges in membrane fabrication – A review. J Memb Sci. 2021;629:119292. doi: 10.1016/j.memsci.2021.119292.

[38] Lim YJ, Goh K, Wang R. The coming of age of water channels for separation membranes: from biological to biomimetic to synthetic. Chem Soc Rev. 2022;51:4537–82. doi: 10.1039/d1cs01061a.

[39] Remanan S, Padmavathy N, Ghosh S, Mondal S, Bose S, Das NC. Porous graphene-based membranes: preparation and properties of a unique two-dimensional nanomaterial membrane for water purification. Sep Purif Rev. 2021; 50:262–82. doi: 10.1080/15422119.2020.1725048.

[40] Gao H, Wang J, Zhang X, Hu M, Xu Q, Xie Y, et al. Confined lamellar channels structured by multilayer graphene for high-efficiency desalination. Desalination. 2022;530:115681.doi:10.1016/j.desal.2022.115681

[41] Understanding the Aqueous Stability and Filtration Capability of MoS$_2$ Membranes Zhongying Wang, Qingsong Tu, Sunxiang Zheng, Jeffrey J. Urban, Shaofan Li, and Baoxia Mi Nano Letters 2017 17(12), 7289-7298 DOI: 10.1021/acs.nanolett.7b02804

[42] Y. Jiao, Y. Zheng, M. Jaroniec, S. Z. Qiao, Design of electrocatalysts for oxygen- and hydrogen-involving energy conversion reactions. Chem. Soc. Rev. 44, 2060–2086 (2015). doi: 10.1039/C4CS00470A; PMID: 25672249

[43] Y. Jiao, Y. Zheng, M. Jaroniec, S. Z. Qiao, Design of electrocatalysts for oxygen- and hydrogen-involving energy conversion reactions. Chem. Soc. Rev. 44, 2060–2086 (2015).doi: 10.1039/C4CS00470A; pmid: 25672249

[44] J. D. Benck, T. R. Hellstern, J. Kibsgaard, P. Chakthranont, T. F. Jaramillo, Catalyzing the hydrogen evolution reaction (HER) with molybdenum sulfide nanomaterials. ACS Catal. 4, 3957–3971 (2014). doi: 10.1021/cs500923c

[45] B. Hinnemann et al., Biomimetic hydrogen evolution: MoS$_2$ nanoparticles as catalyst for hydrogen evolution. J. Am. Chem. Soc. 127, 5308–5309 (2005). doi: 10.1021/ja0504690; pmid: 15826154

[46] Seh, Zhi Wei, et al. "Combining Theory and Experiment in Electrocatalysis: Insights into Materials Design." *Science (American Association for the Advancement of Science)*, vol. 355, no. 6321, 2017, https://doi.org/10.1126/science.aad4998.

[47] Guo, Wei, et al. "Comparative Life Cycle Assessment of Sodium-Ion and Lithium Iron Phosphate Batteries in the Context of Carbon Neutrality." *Journal of Energy Storage*, vol. 72, 2023, pp. 108589-, https://doi.org/10.1016/j.est.2023.108589.

[48] Wickerts, Sanna, et al. "Prospective Life Cycle Assessment of Sodium-ion Batteries Made from Abundant Elements." *Journal of Industrial Ecology*, vol. 28, no. 1, 2024, pp. 116–29, https://doi.org/10.1111/jiec.13452.

[49] Fleischmann, Simon, et al. "Pseudocapacitance: From Fundamental Understanding to High Power Energy Storage Materials." *Chemical Reviews*, vol. 120, no. 14, 2020, pp. 6738–82, https://doi.org/10.1021/acs.chemrev.0c00170.

[50] Zheng, Zhikun, et al. "Synthetic Two-Dimensional Materials: A New Paradigm of Membranes for Ultimate Separation." Advanced Materials (Weinheim), vol. 28, no. 31, 2016, pp. 6529–45, https://doi.org/10.1002/adma.201506237.

[51] Wang, Zhongying, and Baoxia Mi. "Environmental Applications of 2D Molybdenum Disulfide (MoS$_2$) Nanosheets." *Environmental Science & Technology*, vol. 51, no. 15, 2017, pp. 8229–44, https://doi.org/10.1021/acs.est.7b01466.

[52] Liu, C.;Wang, L.; Tang, Y.; Luo, S.; Liu, Y.; Zhang, S.; Zeng, Y.; Xu, Y. Vertical single or few-layer MoS$_2$ nanosheets rooting into TiO$_2$ nanofibers for highly efficient photocatalytic hydrogen evolution. Appl. Catal. B-Environ. 2015, 164, 1–9.

[53] Li, Zizhen, et al. "Recent Development on MoS$_2$-Based Photocatalysis: A Review." *Journal of Photochemistry and Photobiology. C, Photochemistry Reviews*, vol. 35, 2018, pp. 39–55, https://doi.org/10.1016/j.jphotochemrev.2017.12.002.

[54] Wang, Guowei, et al. "Direct Synthesis of Stable 1T-MoS$_2$ Doped with Ni Single Atoms for Water Splitting in Alkaline Media." Small (Weinheim an Der Bergstrasse, Germany), vol. 18, no. 16, 2022, pp. e2107238-n/a, https://doi.org/10.1002/smll.202107238.

[55] Opetubo, Oriyomi Rasak, Kitalu, Ricin, Oviroh, Peter Ozaveshe, Oyinbo, Sunday Temitope, Imoisili, Patrick Ehi and Jen, Tien-Chien. "A mini-review on MoS2 membrane for water desalination: Recent development and challenges" Nanotechnology Reviews, vol. 12, no. 1, 2023, pp. 20220563. https://doi.org/10.1515/ntrev-2022-0563

[56] Wang, Longlu; Zhang, Qingfeng; Zhu, Jingyi; Duan, Xidong; Xu, Zhi; Liu, Yutang; Yang, Hongguan; Lu, Bingan . (2019). *Nature of extra capacity in MoS 2 electrodes: Molybdenum atoms accommodate with lithium. Energy Storage Materials, 16(), 37– 45.* doi:10.1016/j.ensm.2018.04.025.

[57] Manyepedza, Tshiamo, et al. "Impact Electrochemistry of MoS2: Electrocatalysis and Hydrogen Generation at Low Overpotentials." *Journal of Physical Chemistry. C*, vol. 126, no. 42, 2022, pp. 17942–51, https://doi.org/10.1021/acs.jpcc.2c06055.

[58] Wang, Shuai, et al. "Ultrastable In-Plane 1T–2H MoS2 Heterostructures for Enhanced Hydrogen Evolution Reaction." *Advanced Energy Materials*, vol. 8, no. 25, 2018, https://doi.org/10.1002/aenm.201801345.

[59] Fang, Yuqiang, et al. "Structural Determination and Nonlinear Optical Properties of New 1T'''-Type MoS 2 Compound." *Journal of the American Chemical Society*, vol. 141, no. 2, 2019, pp. 790–93, https://doi.org/10.1021/jacs.8b12133.

[60] Eda, Goki, et al. "Photoluminescence from Chemically Exfoliated MoS2." *Nano Letters*, vol. 11, no. 12, 2011, pp. 5111–16, https://doi.org/10.1021/nl201874w.

[61] Abdel Maksoud, M. I. A., et al. "MoS2-Based Nanocomposites: Synthesis, Structure, and Applications in Water Remediation and Energy Storage: A Review." Environmental Chemistry Letters, vol. 19, no. 5, 2021, pp. 3645–81, https://doi.org/10.1007/s10311-021-01268-x.

[62] Liu, Huaizhi, et al. "Production of Mono- to Few-Layer MoS2 Nanosheets in Isopropanol by a Salt-Assisted Direct Liquid-Phase Exfoliation Method." Journal of Colloid and Interface Science, vol. 515, 2018, pp. 27–31, https://doi.org/10.1016/j.jcis.2018.01.023.

[63] Fan, Xiaobin, et al. "Fast and Efficient Preparation of Exfoliated 2H MoS2 Nanosheets by Sonication-Assisted Lithium Intercalation and Infrared Laser-Induced 1T to 2H Phase Reversion." *Nano Letters*, vol. 15, no. 9, 2015, pp. 5956–60, https://doi.org/10.1021/acs.nanolett.5b02091.

[64] Lee, Young Bum, et al. "Facile Microwave Assisted Synthesis of Vastly Edge Exposed 1T/2H-MoS 2 with Enhanced Activity for Hydrogen Evolution Catalysis." *Journal of Materials Chemistry. A, Materials for Energy and Sustainability*, vol. 7, no. 8, 2019, pp. 3563–69, https://doi.org/10.1039/C8TA12080C.

[65] Liu, Haiyang, et al. "Microwave Hydrothermal Synthesis of 1T@2H−MoS2 as an Excellent Photocatalyst." *ChemCatChem*, vol. 12, no. 3, 2020, pp. 893–902, https://doi.org/10.1002/cctc.201901569.

[66] Microwave-assisted synthesis of 1T MoS2/Cu nanowires with enhanced capacity and stability as anode for LIBs Yue Tiana, Xiaoyan Liua,∗, Xiaoqing Caoa, Dieqing Zhanga, Shuning Xiaoa, Xinru Lib, Zaiyuan, Xianyang Lib, Hexing Lia, https://doi.org/10.1016/j.cej.2019.05.174.

[67] Electrochemical performance of mixed-phase 1T/2H MoS$_2$ synthesized by conventional hydrothermal v/s microwave-assisted hydrothermal method for supercapacitor applications Pawanpreet Kour, Deeksha, Kamlesh Yadav* https://doi.org/10.1016/j.jallcom.2022.166194

[68] Solomon, Getachew, et al. "Microwave-Assisted vs. Conventional Hydrothermal Synthesis of MoS 2 Nanosheets: Application towards Hydrogen Evolution Reaction." *Crystals (Basel)*, vol. 10, no. 11, 2020, https://doi.org/10.3390/cryst10111040.

[69] Electrochemical and Optical Properties of Microwave Assisted MoS$_2$ Nanospheres for Solar Cell Application ShreyaSharma, Peeyush Phogat, Ranjana Jha, Sukhvir Singh, doi: 10.12720/sgce.12.3.66-72

[70] Saxena, Mukul, et al. "Microwave-Assisted Synthesis, Characterization and Tribological Properties of a g-C3N4/MoS2 Nanocomposite for Low Friction Coatings." *Coatings (Basel)*, vol. 12, no. 12, 2022, pp. 1840-, https://doi.org/10.3390/coatings12121840.

[71] Amreen Saifi, Prachi Singhal, Sunita Rattan; MoS2/NGP hierarchical hybrid composites synthesized via in–situ microwave method. AIP Conf. Proc. 4 May 2020; 2220 (1): 020147. https://doi.org/10.1063/5.0001679

[72] Nurul Hazwani Aminuddin Rosli, Kam Sheng Lau, Tan Winie, Siew Xian Chin, Sarani Zakaria, Chin Hua Chia, Rapid microwave synthesis of molybdenum disulfide-decorated reduced-graphene oxide nanosheets for use in high electrochemical performance supercapacitors, Journal of Energy Storage, Volume 52, Part C, 2022, 104991, ISSN 2352-152X, https://doi.org/10.1016/j.est.2022.104991.

[73] Gupta, Jyoti, et al. "Microwave Assisted Synthesis of Molybdenum Disulphide/Tungsten Trioxide/Reduced Graphene Oxide (MoS2/WO3/RGO) Nanocomposites for Organic Vapor Sensing." *IOP Conference Series. Materials Science and Engineering*, vol. 1225, no. 1, 2022, pp. 12001-, https://doi.org/10.1088/1757-899X/1225/1/012001.

[74] Fu, Min, et al. "Microwave-Assisted Synthesis of MoS2/Graphene Composites for Supercapacitors." *Journal of Materials Science*, vol. 55, no. 34, 2020, pp. 16385–93, https://doi.org/10.1007/s10853-020-05201-5.

[75] One-step microwave synthesis of MoS2/MoO3@graphite nanocomposite as an excellent electrode material for supercapacitors, Yunrui Tian1 & Xing Yang1 & Amit Nautiyal2 & Yayun Zheng1 & Qingping Guo1 & Jujie Luo & Xinyu Zhang, https://doi.org/10.1007/s42114-019-0075-4

[76] Microwave synthesized self-standing electrode of MoS2 nanosheets assembled on graphene foam for high-performance Li-Ion and Na-Ion batteries Jianyong Xiang*, Dandan Dong, Fusheng Wen, Jing Zhao, Xiaoyan Zhang, Limin Wang, Zhongyuan Liu, http://dx.doi.org/10.1016/j.jallcom.2015.11.040

[77] VOLLATH, D., and D. V. SZABO. "Synthesis of Nanocrystalline MoS2 and WS2 in a Microwave Plasma." Materials Letters, vol. 35, no. 3–4, 1998, pp. 236–44, https://doi.org/10.1016/s0167-577x(97)00247-4.

[78] Acerce, Muharrem, et al. "Metallic 1T Phase MoS2 Nanosheets as Supercapacitor Electrode Materials." Nature Nanotechnology, vol. 10, no. 4, 2015, pp. 313–18, https://doi.org/10.1038/nnano.2015.40.

[79] Geng, Xiumei, et al. "Freestanding Metallic 1T MoS2 with Dual Ion Diffusion Paths as High Rate Anode for Sodium-Ion Batteries." *Advanced Functional Materials*, vol. 27, no. 40, 2017, https://doi.org/10.1002/adfm.201702998.

[80] Benck, Jesse D., et al. "Catalyzing the Hydrogen Evolution Reaction (HER) with Molybdenum Sulfide Nanomaterials." *ACS Catalysis*, vol. 4, no. 11, 2014, pp. 3957–71, https://doi.org/10.1021/cs500923c.

[81] Zhu, Jianqi & Wang, Zhi-Chang & Dai, Huijia & Wang, Qinqin & Yang, Rong & Yu, Hua & Liao, Mengzhou & Zhang, Jing & Chen, Wei & Wei, Zheng & Li, Na & Du, Luojun & Shi, Dong-Xia & Wang, Wenlong & Zhang, Lixin & Jiang, Ying & Zhang, Guangyu. (2019). Boundary activated hydrogen evolution reaction on monolayer MoS2. Nature Communications. 10. 10.1038/s41467-019-09269-9.

[82] Reddy Inta, Harish, et al. "Ionic Liquid-Intercalated Metallic MoS 2 as a Superior Electrode for Energy Storage Applications." *ChemNanoMat : Chemistry of Nanomaterials for Energy, Biology and More*, vol. 6, no. 4, 2020, pp. 685–95, https://doi.org/10.1002/cnma.202000005.

[83] Lukowski, Mark A., et al. "Enhanced Hydrogen Evolution Catalysis from Chemically Exfoliated Metallic MoS2 Nanosheets." Journal of the American Chemical Society, vol. 135, no. 28, 2013, pp. 10274–77, https://doi.org/10.1021/ja404523s.

[84] Sun, Luwei, et al. "ChemInform Abstract: Laminar MoS2 Membranes for Molecule Separation." ChemInform, vol. 45, no. 4, 2014, p. no-no, https://doi.org/10.1002/chin.201404212.

[85] Song, Zailing, et al. "Comparison of Water Desalination Performance of Porous Graphene and MoS2 Nanosheets." *RSC Advances*, vol. 12, no. 42, 2022, pp. 27641–47, https://doi.org/10.1039/d2ra04544c.

[86] https://www.vacuumfiltrations.com

[87] https://serc.carleton.edu/research_education/geochemsheets/BraggsLaw.html

[88] Sethi, Meenaketan, et al. "A Porous Graphene-NiFe2O4 Nanocomposite with High Electrochemical Performance and High Cycling Stability for Energy Storage Applications." *Nanoscale Advances*, vol. 2, no. 9, 2020, pp. 4229–41, https://doi.org/10.1039/d0na00440e.

[89] S. Ardizzone, G. Fregonara, S. Trasatti, Electrochim. Acta. 35 (1) (1990) 263 267.

[90] Shao, Hui, et al. "Electrochemical Study of Pseudocapacitive Behavior of Ti3C2Tx MXene Material in Aqueous Electrolytes." *Energy Storage Materials*, vol. 18, 2019, pp. 456–61, https://doi.org/10.1016/j.ensm.2018.12.017.

[91] Dupont, Madeleine F., and Scott W. Donne. "A Step Potential Electrochemical Spectroscopy Analysis of Electrochemical Capacitor Electrode Performance." *Electrochimica Acta*, vol. 167, 2015, pp. 268–77, https://doi.org/10.1016/j.electacta.2015.03.137.

[92]   Kingsbury, Ryan S., et al. "Junction Potentials Bias Measurements of Ion Exchange Membrane Permselectivity." *Environmental Science & Technology*, vol. 52, no. 8, 2018, pp. 4929–36, https://doi.org/10.1021/acs.est.7b05317.

[93]   AIXALA PERELLO, Anna, et al. *Permselectivity and Ionic Conductivity Study of Na+ and Br− Ions in Graphene Oxide-Based Membranes for Redox Flow Batteries*. 2023.

[94]   AIXALA PERELLO, Anna, et al. *Scalable and Highly Selective Graphene-Based Ion-Exchange Membranes with Tunable Permselectivity*. 2023.

[95]   Abbas, Z., Ahlberg, E. Activity Coefficients of Concentrated Salt Solutions: A Monte Carlo Investigation. *J Solution Chem* **48**, 1222–1243 (2019). https://doi.org/10.1007/s10953-019-00905-y

[96]   [Membrane Science and Technology] Ion-Exchange Membrane Separation Processes Volume 9 || Chapter 3 Preparation and characterization of ion-exchange membranes. 89–146. doi:10.1016/S0927-5193(04)80034-2

[97]   https://cem.com/it/microwave-chemistry/solvent-choice?___store=it&___from_store=cn

[98]   Shi, Yayun, et al. "Self-Assembled Ultrathick MoS_2 Conductive Hydrogel Membrane via Ionic Gelation for Superior Capacitive Energy Storage." *Chinese Chemical Letters*, 2024, pp. 109772-, https://doi.org/10.1016/j.cclet.2024.109772.

[99]   Thi Xuyen, Nguyen, and Jyh-Ming Ting. "Hybridized 1T/2H MoS_2 Having Controlled 1T Concentrations and Its Use in Supercapacitors." Chemistry : A European Journal, vol. 23, no. 68, 2017, pp. 17348–55, https://doi.org/10.1002/chem.201703690.

[100] https://ravescientific.com/products/high-resolution-fesem-zeiss-sigma

[101] Thombare, Sohan, et al. "Effect of Electrolytes on the Performance of Graphene Oxide Anode Material for Ultracapacitor, Li-Ion Capacitor, and Li-Ion Battery: Three-in-One Approach." *Indian Journal of Physics*, vol. 97, no. 10, 2023, pp. 2927–42, https://doi.org/10.1007/s12648-023-02647-6.

[102] Attanayake, Nuwan H., et al. "Effect of Intercalated Metals on the Electrocatalytic Activity of 1T-MoS_2 for the Hydrogen Evolution Reaction." *ACS Energy Letters*, vol. 3, no. 1, 2018, pp. 7–13, https://doi.org/10.1021/acsenergylett.7b00865.

[103] Cook, John B., et al. "Pseudocapacitive Charge Storage in Thick Composite MoS_2 Nanocrystal-Based Electrodes." *Advanced Energy Materials*, vol. 7, no. 2, 2017, https://doi.org/10.1002/aenm.201601283.

[104] Zhou, Xiaoyu, et al. "Significantly Increased Raman Enhancement on Defect-Rich O-Incorporated 1T-MoS_2 Nanosheets." *Journal of Materials Science*, vol. 55, no. 34, 2020, pp. 16374–84, https://doi.org/10.1007/s10853-020-05172-7.

[105] Aixalà-Perelló, Anna, et al. "Enhancing Surface Charge Density of Graphene Oxide Membranes through $Al(OH)_4^-$ Anion Incorporation for Osmotic Energy Conversion." *Advanced Energy and Sustainability Research*, vol. 5, no. 9, 2024, https://doi.org/10.1002/aesr.202400090.

[106] Lu, X. et al. Relating selectivity and separation performance of lamellar two-dimensional molybdenum disulfide (MoS_2) membranes to nanosheet stacking behavior. Environ. Sci. Technol. https://doi.org/10.1021/acs.est.0c02364 (2020).

[107] Cook, John B., et al. "Mesoporous MoS$_2$ as a Transition Metal Dichalcogenide Exhibiting Pseudocapacitive Li and Na-Ion Charge Storage." *Advanced Energy Materials*, vol. 6, no. 9, 2016, https://doi.org/10.1002/aenm.201501937.

[108] Parthiban Pazhamalai, et al. "Supercapacitive Properties of Amorphous MoS3 and Crystalline MoS$_2$ Nanosheets in an Organic Electrolyte." *Inorganic Chemistry Frontiers*, vol. 6, no. 9, 2019, pp. 2387–95, https://doi.org/10.1039/c9qi00623k.

[109] Wu, Tongxia. "Electrochemical Study on Mixture of 1M LiPF6 and Carbonate Solvents as an Electrolyte in Graphite/ Lithium and Graphene/ Lithium-Ion Batteries." *International Journal of Electrochemical Science*, vol. 17, no. 11, 2022, pp. 221171-, https://doi.org/10.20964/2022.11.59.

[110] Niaz, Niaz Ahmad, et al. "Improved Structural, Electronic, and Electrochemical Properties of MoS2/Graphene Oxide Composite for Li-Ion Batteries Applications." *Journal of Materials Science. Materials in Electronics*, vol. 34, no. 28, 2023, pp. 1942-, https://doi.org/10.1007/s10854-023-11212-0.

[111] Wang, Monong, et al. "Heterogeneous MoS2-GO Membranes with Enhanced Resistance to Swelling and Restacking." *Journal of Membrane Science*, vol. 697, 2024, pp. 122548-, https://doi.org/10.1016/j.memsci.2024.122548.

[112] Gigot, Arnaud, et al. "Mixed 1T–2H Phase MoS$_2$/Reduced Graphene Oxide as Active Electrode for Enhanced Supercapacitive Performance." *ACS Applied Materials & Interfaces*, vol. 8, no. 48, 2016, pp. 32842–52, https://doi.org/10.1021/acsami.6b11290.

[113] Wang, Dezhi, et al. "Phase Engineering of a Multiphasic 1T/2H MoS 2 Catalyst for Highly Efficient Hydrogen Evolution." *Journal of Materials Chemistry. A, Materials for Energy and Sustainability*, vol. 5, no. 6, 2017, pp. 2681–88, https://doi.org/10.1039/C6TA09409K.

[114] Chou, Stanley S., et al. "Understanding Catalysis in a Multiphasic Two-Dimensional Transition Metal Dichalcogenide." *Nature Communications*, vol. 6, no. 1, 2015, pp. 8311–8311, https://doi.org/10.1038/ncomms9311.